

Department of Physics and Astronomy
University of Heidelberg

Bachelor Thesis in Physics
submitted by

Lukas Huxold

born in Köln (Germany)

2014

Cooling of the Mu3e Pixel Detector

This Bachelor Thesis has been carried out by

Lukas Huxold

at the

Physikalisches Institut

in Heidelberg

under the supervision of

Dr. Niklaus Berger

Abstract

The Mu3e experiment searches for the decay $\mu^+ \rightarrow e^+e^+e^-$, which is suppressed to unobservable levels in the standard model of particle physics. Therefore an observation of this decay would be a clear hint for new physics. The sensitivity of the Mu3e experiment should ultimately reach one in 10^{16} decays.

To reach the proposed sensitivity, thin High Voltage Monolithic Active Pixel Sensors (HV-MAPS) are used, which are expected to produce heat with a thermal power of 150 mW/cm^2 .

To operate the pixel sensors of the Mu3e detector stably, they have to be actively cooled. In order to reduce the material within the detector acceptance to a minimum, the heat should be carried away by gaseous helium. With the intention to estimate the possibilities of the helium cooling, a heatable model of two detector layers has been built and then cooled by an air flux, while the temperature on the surfaces has been measured. Simulations of both air cooling and gaseous helium cooling have been carried out.

Zusammenfassung

Das Mu3e Experiment sucht, nach dem Teilchenzerfall $\mu^+ \rightarrow e^+e^+e^-$, der nach dem Standardmodell der Teilchenphysik weit über die Grenzen der Messbarkeit hinaus unterdrückt ist. Ein Nachweis dieses Zerfalls wäre also ein klarer Hinweis auf neue Physik. Die angestrebte Sensitivität des Mu3e Experimentes liegt bei einem in 10^{16} Zerfällen.

Um diese angestrebte Sensitivität erreichen zu können, wird auf neuartige, mit Hochspannung betriebene, „Monolithische Aktive Pixelsensoren“ (HV-MAPS) gesetzt. Die erwartete Wärmeleistung durch die im Sensor integrierten Schaltungen ist ca. 150 mW/cm^2 .

Um die Pixelchips des Mu3e Detektors sinnvoll betreiben zu können, müssen diese aktiv gekühlt werden. Da auf so viel wie möglich Material innerhalb des Detektors verzichtet werden muss, soll mit gasförmigem Helium Wärme abtransportiert werden. Um die Kühlmöglichkeiten mit dem Heliumstrom einschätzen zu können, ist ein heizbares Modell zweier Pixel-Lagen des Detektors konstruiert worden, welches zunächst mit einem Luftstrom gekühlt wurde, während die Temperatur entlang der Oberflächen gemessen wurde. Computersimulationen sowohl der Luftkühlung als auch der Kühlung mit gasförmigem Helium wurden zum Vergleich durchgeführt.

Contents

Abstract	5
List of Figures	11
List of Tables	13
1 Introduction	15
2 The Mu3e Experiment	17
2.1 Motivation	17
2.2 Detector Design and Working Principle	18
3 Experimental Setup	23
3.1 Heatable Model	23
3.1.1 Thin Foil Heating	24
3.1.2 Thick Foil Heating	26
3.1.3 Support Structure	32
3.1.4 Assembling Of The Model	33
3.2 Temperature Data Acquisition	36
3.2.1 Resistance Thermometer	37
3.2.2 LabVIEW Program	41
3.3 Flow Reactor	41
4 Measurements	43
4.1 Auxiliary Measurements	44
4.1.1 Calibration	44
4.1.2 Air Speed	45
4.2 Main Measurements	47
4.2.1 Measurements Without Air Flow	47
4.2.2 Measurements With Air Flow	49

5	Simulations	59
5.1	Simulations With Air	61
5.1.1	Temperature Profiles	61
5.1.2	Air Speed Projection	65
5.2	Simulations With Helium	66
5.2.1	Temperature Profiles	67
5.2.2	Helium Speed Projection	71
5.3	Comparison	72
5.4	Further Simulations	75
6	Conclusion and Outlook	77
7	Acknowledgements	81

List of Figures

2.1	Mu3e logo	17
2.2	Feynman diagrams of muon decays in SM	18
2.3	Feynman diagrams of muon decays in SM extensions	18
2.4	Basic Detector Design	19
2.5	Missing energy helps to discriminate between $\mu \rightarrow eee$ and $\mu \rightarrow eee\nu_e\bar{\nu}_\mu$ decays	20
2.6	Mechanical Prototype	21
3.1	Complete experimental setup	23
3.2	Pattern for the heating foil	28
3.3	Absorption spectrum of aluminium and other metals.	29
3.4	Laser tuning pattern	30
3.5	Results of the laser and manual processing	32
3.6	Connectors on the thick foil	33
3.7	Foil supporting framework	34
3.8	Aluminium end-rings with connector support structure.	35
3.9	Sensors on the inner layer	36
3.10	Temperature sensors glued on an outer foil with thermally conductive glue.	37
3.11	Comparison of the exact IEC/DIN formula (3.19) : $T_1(R)$ and the linear approximation (3.20) : $T_2(R)$	39
3.12	The anemometer.	42
4.1	Calibration of a sensor	45
4.2	Air speed fluctuations.	47
4.3	Temperature profiles at different powers without air flow.	48
4.4	The mean temperature at different powers without air flow.	49
4.5	Temperature profiles on 4 th layer, upside, at 100 mW/cm ² and different air speeds.	50

4.6	Temperature profiles on 4 th layer, upside, at 150 mW/cm ² and different air speeds and two fits to determine the temperature gradient.	51
4.7	Temperature profiles at 150 mW/cm ² on the side of the 4 th layer.	52
4.8	Temperature profiles at 150 mW/cm ² on the bottom of the 4 th layer.	53
4.9	Comparison of the profiles for different positions in φ	53
4.10	Temperature profile on the inner layer at the “top”-position heated with 150 mW/cm ² and cooled with different air speeds.	54
4.11	Air speed dependence of the maximum temperature on the top of the 4 th layer.	55
4.12	Air speed dependence of the maximum temperature on the side of the 4 th layer.	56
4.13	Air speed dependence of the maximum temperature on the bottom of the 4 th layer.	57
4.14	The temperature gradient on the top 4 th layer dependent to the air speed.	57
5.1	The CAD design for the CFD simulations.	60
5.2	Thermal images of the model cooled with air. For easy comparison the temperature range is the same in both images: from 20 °C to 170 °C.	62
5.3	Temperature profiles on the 4 th layer obtained from the simulations with air flow.	63
5.4	Temperature profiles on the 3 rd layer obtained from the simulations with air flow.	63
5.5	Temperature profiles on the 3 rd and 4 th layer on the top, side and bottom position at 3.5 m/s air speed.	64
5.6	The maximum temperature on the top of the model in dependence of the air speed.	65
5.7	Comparison of maximum temperatures measured and simulated.	66
5.8	Thermal images of the model cooled with helium. For easy comparison the temperature range is the same as for the air cooling before: from 20 °C to 170 °C.	68
5.9	Temperature profiles on the 4 th layer obtained from the simulations with helium flow.	69
5.10	Temperature profiles on the 3 rd layer obtained from the simulations with helium flow.	69
5.11	Temperature profiles on the 3 rd and 4 th layer on the top, side and bottom position at 3.5 m/s helium speed.	70

5.12	The maximum temperature on the top of the model in dependence of the helium speed.	71
5.13	Comparison of the flow speed and medium dependence of the maximum temperature.	73
5.14	Comparison of temperature profiles obtained from simulations with air and with helium.	74
5.15	Thermal images of the more detailed 3 rd layer model	75

List of Tables

3.1	Laser parameters	30
3.2	Resistances of the foils at 20°C.	31
4.1	Calibration parameters for the Pt1000 sensors.	46
4.2	Powers used for the measurements without air flow. P/F is the power per foil.	47
4.3	Powers used for the measurements with air flow. P/F is the power per foil.	49
4.4	Temperature gradients on the top 4 th layer for different air speeds.	56
5.1	Fit parameters.	72

1 Introduction

The standard model of particle physics (SM) has been very successful in explaining elementary particles and their interactions. One of the greatest successes might be the discovery of the Higgs boson in 2013, making the SM complete. Despite the great successes, there are still unexplained phenomena and experimental results, which begs the question of physics beyond the SM. One observed phenomenon, which is not compatible with the SM is neutrino oscillation. Contrary to the SM prediction the lepton flavour is not conserved for the (electrically) uncharged leptons. Until today a violation of the flavour of the (electrically) charged leptons (CLFV) has not been observed. Finding such a violation would be a clear evidence for new physics beyond the SM.

Several experiments are performed or planned to search for charged lepton flavour violation (CLFV). One of them is the Mu3e experiment, which will search for the $\mu \rightarrow eee$ decay [1]. The SINDRUM experiment already searched for this decay¹ excluding it down to a branching ratio of $BR(\mu^+ \rightarrow e^+e^+e^-) < 1 \cdot 10^{-12}$ [2]. The aimed sensitivity of the Mu3e experiment of one in 10^{16} decays is a factor of 10000 higher, which requires a high muon decay rate. Currently up to $10^8 \mu$ per second are available at the Paul Scherrer Institute (PSI). A future high intensity muon beam line (HiMB) could provide in excess of $10^9 \mu$ per second, sufficient for reaching the planned sensitivity. To distinguish between the $\mu \rightarrow eee$ signal and the standard model allowed $\mu \rightarrow eee\nu\bar{\nu}$ decay, the momentum of the electrons has to be determined very precisely. Considering this and the high rate, which can lead to background from accidental combinations from independent muon decays, today's detector method of choice is a combination of scintillating tiles and fibres and novel High Voltage Monolithic Active Pixel Sensors (HV-MAPS).

The HV-MAPS have the great advantage that they can be thinned to $50 \mu\text{m}$ and do not need additional readout chips in the active volume. In this way they cause little multiple scattering and thus are excellent for momentum resolution. The integrated active electronics, however, heats the chips.

For a planned readout design of the HV-MAPS providing a time resolution of $\approx 14 \text{ ns}$ a

¹From 1983 to 1986 at the Paul Scherrer Institute.

power consumption of 150 mW/cm^2 is expected [1].

Without any external cooling, the Detector would heat up to temperatures which destroy the sensors. An operating temperature lower than 70°C is required and temperature gradients should be as small as possible. Since a large amount of material within the detector has to be avoided, cooling with gaseous helium has been proposed. Studies on cooling a single sensor with gaseous helium have been performed [3]. Therefore the next step was to develop an experimental setup allowing studies on a bigger substructure of the full pixel detector, which will be the topic of this thesis. The experimental setup includes a model of the 3^{rd} and 4^{th} layer of the central pixel detector of the Mu3e experiment, which can be heated and cooled.

2 The Mu3e Experiment

The Mu3e experiment has been approved in January 2012 and will take place at the Paul Scherrer Institute in Switzerland. It aims to search for the charged lepton flavour violating decay $\mu^+ \rightarrow e^+e^+e^-$ with a branching ratio sensitivity of 10^{-16} at 90% confidence level [1]. This will improve the sensitivity reached by the SINDRUM experiment [2], which did not find any $\mu^+ \rightarrow e^+e^+e^-$ decay, by four orders of magnitude.



Figure 2.1: Mu3e logo

2.1 Motivation

The main observed decay channel for μ^+ are $\mu^+ \rightarrow e^+\nu_e\bar{\nu}_\mu$, shown in Fig. 2.2a, with a branching ratio of nearly 100%, $\mu^+ \rightarrow e^+\nu_e\bar{\nu}_\mu\gamma$ with a branching ratio of $1.4(4) \cdot 10^{-2}$ and $\mu^+ \rightarrow e^+e^+e^-\nu_e\bar{\nu}_\mu$, shown in Fig. 2.2b, with a branching ratio of $3.4(4) \cdot 10^{-5}$ [4]. For these decay channels the number of leptons of each flavour is conserved. Therefore, they are allowed (and predicted) in the SM which includes lepton flavour conservation.

A less strict lepton flavour conservation is given in the ν SM, which is an extension of the SM. The ν SM allows neutrino oscillations so that the decay $\mu^+ \rightarrow e^+e^+e^-$ would be allowed based on neutrino mixing (Fig. 2.3a) although it is suppressed to an unobservable branching ratio of $\approx 10^{-54}$. Therefore, neither SM nor ν SM could explain the $\mu^+ \rightarrow e^+e^+e^-$ decay, if it is found within the sensitivity of the Mu3e experiment.

There are many theories of physics beyond the SM predicting additional lepton flavour violating processes, including the $\mu \rightarrow eee$ decay. An example are the SUSY (supersymmetric) extensions of the SM. A possible $\mu^+ \rightarrow e^+e^+e^-$ decay in SUSY is shown in Fig. 2.3b.

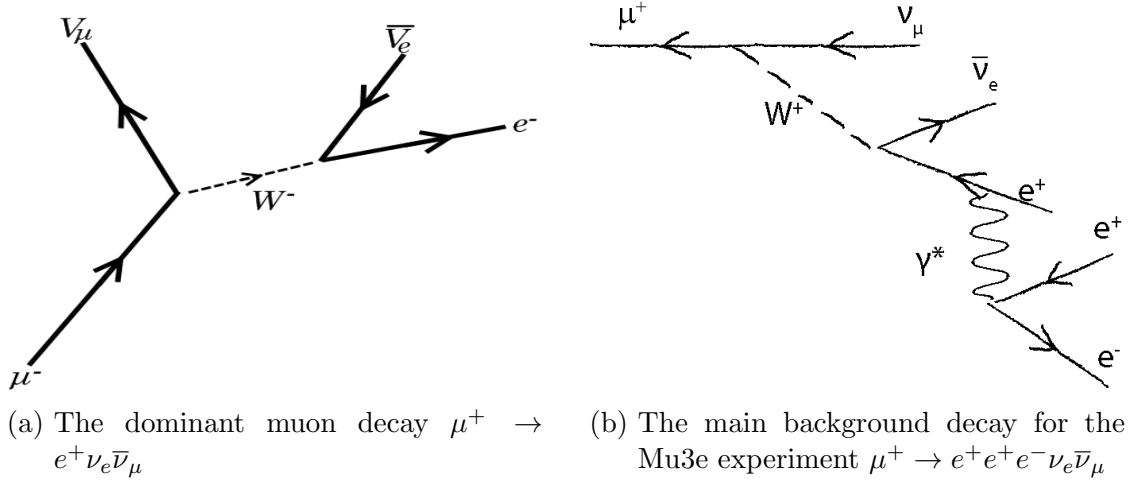


Figure 2.2: Feynman diagrams of muon decays in SM

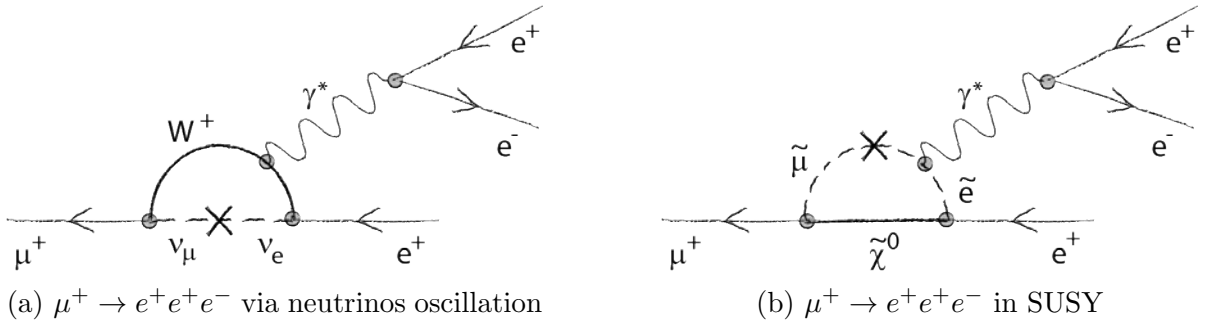


Figure 2.3: Feynman diagrams of muon decays in SM extensions

2.2 Detector Design and Working Principle

The basic detector design is sketched in Fig. 2.4. A beam of muons¹ will be stopped on a hollow double cone target made of aluminium, which sits at the center of the detector. Around the target there are two double layers of HV-MAPS. One pair close to the target, which is necessary to determine the vertex position of a decay and another pair further outside, which will determine the tracks of the decay products together with the inner pair. Just inside the inner layer of the outer pair, scintillating fibres will be positioned, helping to increase the time resolution. The detector will be enclosed in a superconducting magnet, which generates a solenoidal magnetic field of 1 T.

When the muons are stopped on the target, they will decay at rest. Thus the vectorial

¹With muon rates from $(10^7 - 10^8)\mu/s$ for phase I and up to $2 \cdot 10^9\mu/s$ for phase II.

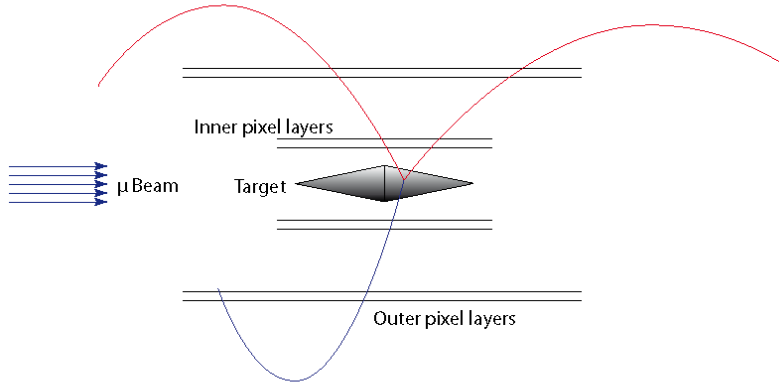


Figure 2.4: The basic detector design of the Mu3e experiment in phase IA

sum of momenta of the N decay products in the laboratory frame has to vanish:

$$\sum_{i=1}^N \vec{p}_i = 0. \quad (2.1)$$

Furthermore the invariant mass of the decay products has to equal the muon rest mass:

$$\left(\sum_{i=1}^N \mathbf{P}_i \right)^2 = m_\mu^2 c^4 \quad (\approx (105.7 \text{ MeV})^2). \quad (2.2)$$

Taking (2.1) and (2.2) into account, the energy for a single electron (positron) of a $\mu \rightarrow eee$ decay can only be between 0.5 MeV and 53 MeV (half the muon mass). Also the initial momenta of the three (anti-)electrons have to be in one plane so that (2.1) is satisfied. After the decay the (anti-)electrons are moving in the solenoidal magnetic field, which bends them into helical tracks [5] with radii depending on their momenta and the magnetic field. Determining the radius of a track therefore will give the momentum of the (anti-)electron moving on this track. Knowing which triplet of (anti-)electrons comes from one vertex gives then the opportunity to build the sum over momenta. If the track belongs to a $\mu^+ \rightarrow e^+e^+e^-\nu_e\bar{\nu}_\mu$ decay (Fig. 2.5), the equations (2.1) and (2.2) will not be satisfied but differ by the momenta and energy of the two neutrinos which are not detected.

Because this thesis will treat the cooling of the outer pixel layers, I will describe them

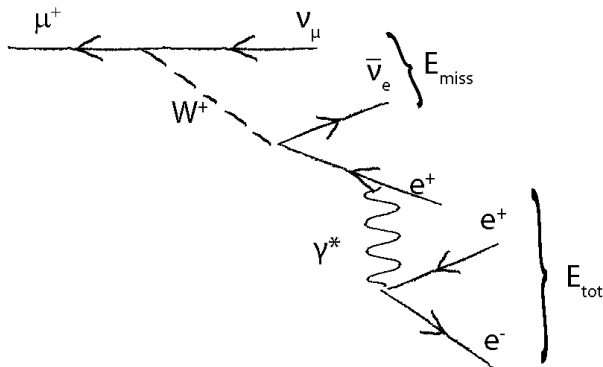


Figure 2.5: Missing energy helps to discriminate between $\mu \rightarrow eee$ and $\mu \rightarrow eee\nu_e\bar{\nu}_\mu$ decays

in more detail. The 3rd layer² will consist of a 24 sided prism with a length of 36 cm and the 4th of a 28 sided one of the same length. Each side will have a width of about 1.9 cm and carry the 2 cm wide HV-MAPS sensors³. The HV-MAPS are radiation-hard pixel sensor chips, which can detect ionising particles when they pass through a pixel. Since active readout electronics are integrated into every pixel, they will consume a significant amount of power of about 150 mW/cm². For the full detector⁴ the total power will therefore be about 3 kW. The released heat will be carried away by a helium flux parallel to the detector axis. Since the HV-MAPS on the four layers are thinned down to 50 μm some kind of support structure is needed. This will be provided by a frame made from Kapton[®], which is a polyimide film with properties suitable for the detector in many ways. The framework consists of a folded and glued Kapton[®]-cylinder, which has hollow prisms on the inside of each side, which will provide more stiffness and will serve as a pipe for an additional helium flux, separated from the main flux around the whole detector.

²Counting the HV-MAPS layers from the inside to the outside

³They will overlap one edge to prevent inactive detector surface.

⁴Phase II with $5 \times 3^{\text{rd}}$ and 4^{th} layer and $1 \times 1^{\text{st}}$ and 2^{nd} layer.

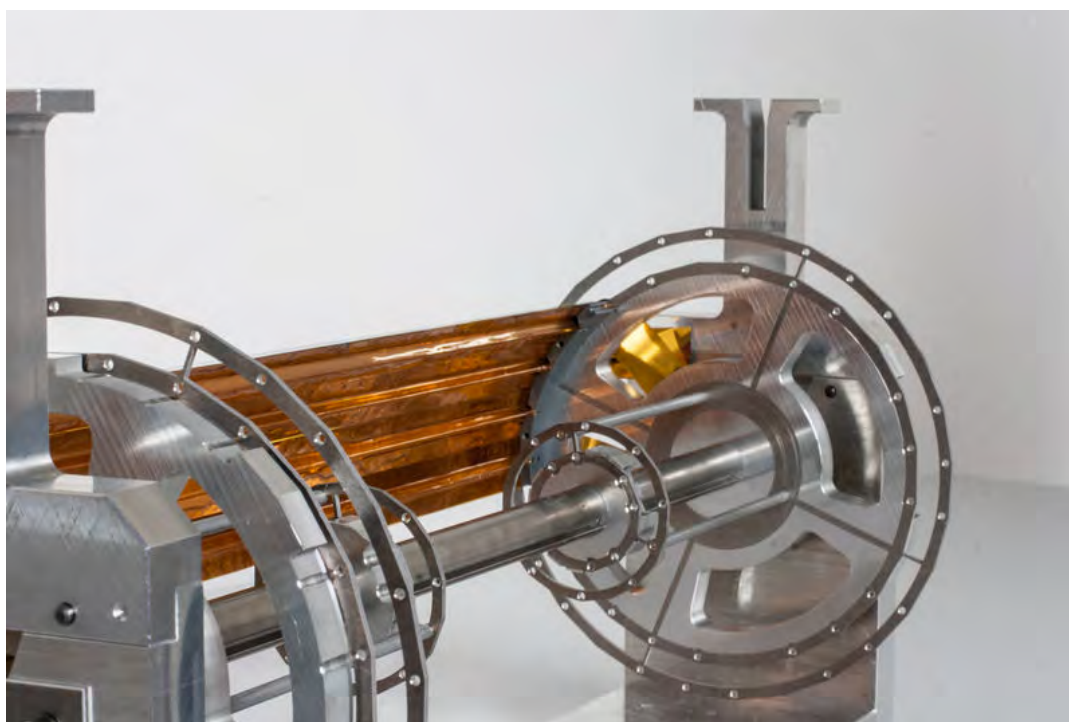


Figure 2.6: Part of a mechanical prototype of the 3rd layer. View on the inside with the Kapton[®]-ducts.

3 Experimental Setup

To investigate the cooling of the outer pixel detector layers, an experimental setup has been developed. It includes a heatable model of the 3rd and 4th layers of the pixel detector, sensors for the temperature measurements and a flow reactor, in which the model is cooled by an air flow. In this chapter the development of the model, the temperature data acquisition and the flow reactor are described. The complete setup is shown in Fig. 3.1.

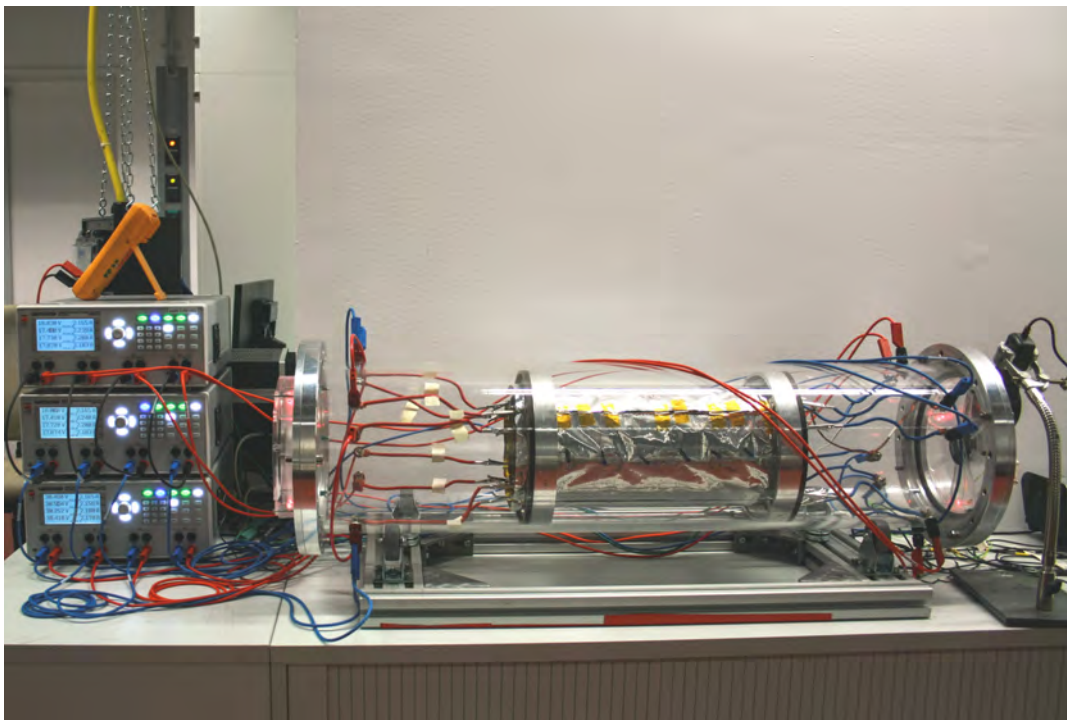


Figure 3.1: The complete setup during a measurement.

3.1 Heatable Model

The model is assembled from heatable foils, a cage structure carrying them, and connectors for the electrical power. In the following, I will give a summary of the development

process of the model and explain how the final setup is constructed.

Since the HV-MAPS in the final detector will be mounted on aluminized Kapton[®], the approach to use the thin aluminium film on these foils as ohmic heating resistor seems to suggest itself. Also it is reasonable to simplify the geometry of the model from 24 and 28 sided prisms to cylinders and split each into four sectors, to be able to split up the powering to 4 sources each.

3.1.1 Thin Foil Heating

The first attempt was made with a foil composed of 25 μm Kapton[®] that is metallized with about 50 nm of aluminium. To roughly estimate the ohmic resistance R of a foil, which could be used for the setup, the following consideration helps. Assuming, the electric current will flow through the film homogeneously over the full width of the foil and aluminium film dimensions of: length $l \approx 36$ cm, width $w \approx 13$ cm, high $h \approx 50$ nm one calculates:

$$R = \rho_{al}^{el} \cdot \frac{l}{A_{\varnothing}} \quad \text{with} \quad A_{\varnothing} = w \cdot h \quad \text{and} \quad \rho_{al}^{el} = 2.6 \cdot 10^{-8} \Omega\text{m} \quad (3.1)$$

$$R = 2.6 \cdot 10^{-8} \cdot \frac{36 \cdot 10^{-2}}{13 \cdot 10^{-2} \cdot 50 \cdot 10^{-9}} \cdot \frac{\Omega\text{m}^2}{\text{m}^2} \quad (3.2)$$

$$R \approx 1.5 \Omega \quad (3.3)$$

Where A_{\varnothing} is the cross-section trough which the current is running and ρ_{al}^{el} is the specific electrical resistance of aluminium. To simulate a power consumption of $150 \text{ mW}/\text{cm}^2$ on this foil, one obtains:

$$P = 150 \text{ mW}/\text{cm}^2 \cdot A \quad \text{with} \quad A = l \cdot w \quad (3.4)$$

$$P = 150 \cdot 36 \cdot 13 \cdot \frac{\text{mW} \cdot \text{cm}^2}{\text{cm}^2} \quad (3.5)$$

$$P \approx 70 \text{ W} \quad (3.6)$$

With the estimated resistance, this leads to voltage V and current I of:

$$P = \frac{U^2}{R} \quad \Rightarrow \quad U = \sqrt{P \cdot R} \quad \Rightarrow \quad U \approx 10 \text{ V} \quad (3.7)$$

$$P = I^2 \cdot R \quad \Rightarrow \quad I = \sqrt{\frac{P}{R}} \quad \Rightarrow \quad I \approx 7 \text{ A} \quad (3.8)$$

At first sight this result has both advantages and disadvantages. An advantage would be that the current and voltage needed match with the specifications of the HAMEG HMP 4040¹ power supply available in the lab. The disadvantage is the quite high current of about 5 A, which leads to significant power consumption on cables and connections, if their resistance is not small enough. This approach is only appropriate if one manages to distribute the current over the full width of the foils. In order to do this, stripes of household aluminium foil (approximately 13 cm × 2 cm × 25 μm) have been glued on both short edges of the aluminized Kapton[®]-foil with electrically conductive glue. With this concept, a complete model² was built by the workshop of the physics institute before I started my work on the project. Unfortunately, this model only was able to endure powers of a few Watts before the aluminium evaporated from the Kapton[®]-foil near to the edges of the household aluminium foil. This is due to the fact that the current seeks the way of lowest resistance. As long as the resistance through the glue isn't small enough, the majority of the current goes through the household foil to the edge to the Kapton[®]-foil and there runs through the glue with a very high current density, which leads to a high local power load that vaporizes the ultra thin aluminium film. In order to maintain the nice concept, a lot of tests to improve the conductivity between the household foil and the aluminized Kapton[®]-foil were made. Approaches to improve the conductivity by trying different thicknesses of conductive glue failed. In contrast, clamping metal chips to the aluminium side of the Kapton[®]-foil was very effective. Since the current still has to be distributed over the full width of the foil this leads to many difficulties with this concept. The two possible approaches would be either to design clamps which follow the radii of the bend foils and have contact to them over their full width or to equip the foils with many small clamps next to each other. Option one would mean a lot of work for the workshop and additional material disturbing the air flow which would distort the measurements. The second option would also lead to more material in the flow which would in addition be irregularly distributed. Besides there

¹A maximum current of 10 A for voltages from 0 V to 16 V and decreasing current to 5 A at maximum voltage of 32 V for each of the 4 channels.

²It is 40 cm long instead of 36 cm to provide space for the current distribution and connections.

would still be a risk for the aluminium to evaporate in spots of high current density. Considering this difficulties it is worth to look for alternative concepts for the heating foil.

3.1.2 Thick Foil Heating

The easiest way to prevent the aluminium film from evaporating is choosing thicker aluminium. For this a foil of 25 μm Kapton[®] laminated with 25 μm aluminium was available. Considering equation (3.1) one can easily calculate that the resistance of this foil used like the thin foil before would be extremely small, meaning one would need very high currents to reach the aimed power consumption:

$$R \approx 3 \text{ m}\Omega \quad \Rightarrow U \approx 0.45 \text{ V} \quad \Rightarrow I \approx 156 \text{ A} \quad (3.9)$$

With the available power supplies, cables and connectors, this is not a viable option. Since we do not want (and cannot) lower the thickness, the two parameters left are length and width. Of course neither simply stretching the model by a huge factor nor making a lot of very small single stripes which are powered separately would be practical. Therefore the only reasonable approach is to build something like a long wire of small stripes after each other. One way to do this would be to cut the foil into small stripes and then connect them alternating on the ends. This would clearly be a mechanically unstable design. Another way is to create a pattern on the foil, by taking away aluminium between the stripes without removing the Kapton[®] substrate. Since one can not simply scratch away 25 μm of aluminium or cut it without destroying the Kapton[®], one has to use another technique. Laser cutting resp. engraving seemed worth a consideration, since the PI workshop recently obtained a laser cutter for this purpose.

Design Of The Heating Pattern

In order to reduce the currents and therefore the unwanted power consumption of the cables and connectors, but still stay inside of the voltage limit³ of the power supplies, the following calculations were made:

³ $U_{max} = 32 \text{ V}$ but for some safety margin $U = 30 \text{ V}$ was aimed for.

$$P = \frac{U^2}{R} = 150 \text{ mW/cm}^2 \cdot A_{foil} \quad (3.10)$$

$$\Rightarrow R = \frac{U^2}{150 \text{ mW/cm}^2 \cdot A_{foil}} \quad (3.11)$$

So the pattern should be dimensioned like:

$$R = \rho_{al}^{el} \cdot \frac{\tilde{l}}{A_{\varnothing}} \quad \text{with} \quad A_{\varnothing} = \tilde{w} \cdot h \quad \text{and} \quad \tilde{l} \cdot \tilde{w} = A_{foil} = l \cdot w \quad (3.12)$$

$$\Rightarrow R = \rho_{al}^{el} \cdot \frac{\tilde{l}}{\tilde{w} \cdot h} = \rho_{al}^{el} \cdot \frac{l \cdot w}{\tilde{w}^2 \cdot h} \quad (3.13)$$

$$\Rightarrow \tilde{w} = \sqrt{\rho_{al}^{el} \cdot \frac{A_{foil}}{R \cdot h}} \quad (3.14)$$

$$\Rightarrow \tilde{w} = \sqrt{\rho_{al}^{el} \cdot \frac{A_{foil}^2 \cdot 150 \text{ mW/cm}^2}{U^2 \cdot h}} \quad (3.15)$$

Where the tilded l and w are the length and width of the pattern stripes while the untilded ones describe the foil. For $\rho_{al}^{el} = 2.6 \cdot 10^{-8} \Omega\text{m}$, $h = 25 \mu\text{m}$, $l = 40 \text{ cm}$, $w = 13 \text{ cm}$ and $U = 30 \text{ V}$ we get:

$$\tilde{w} \approx 2.2 \text{ mm}$$

Still this is just a rough estimation, since no reserved space for connectors and no space between the stripes were taken into account. Because both aspects will lower the resistance a stripe width of $\tilde{w} = 2 \text{ mm}$ with a linewidth between the stripes of $d = 0.5 \text{ mm}$ were chosen and the pattern shown in Fig. 3.2 were prepared. The pattern for the foils for the 3rd layer only differs from it by the width of the foil which equals 11 cm (instead of 13 cm for foils for the 4th layer).

Lasering Of The Pattern

As already mentioned it is quite difficult to remove a layer of 25 μm aluminium from a Kapton[®]-foil of the same thickness without destroying the foil. One possible way is to evaporate the aluminium by depositing energy locally into the aluminium. This is realized by laser cutters which are commercially available. Recently, the institute

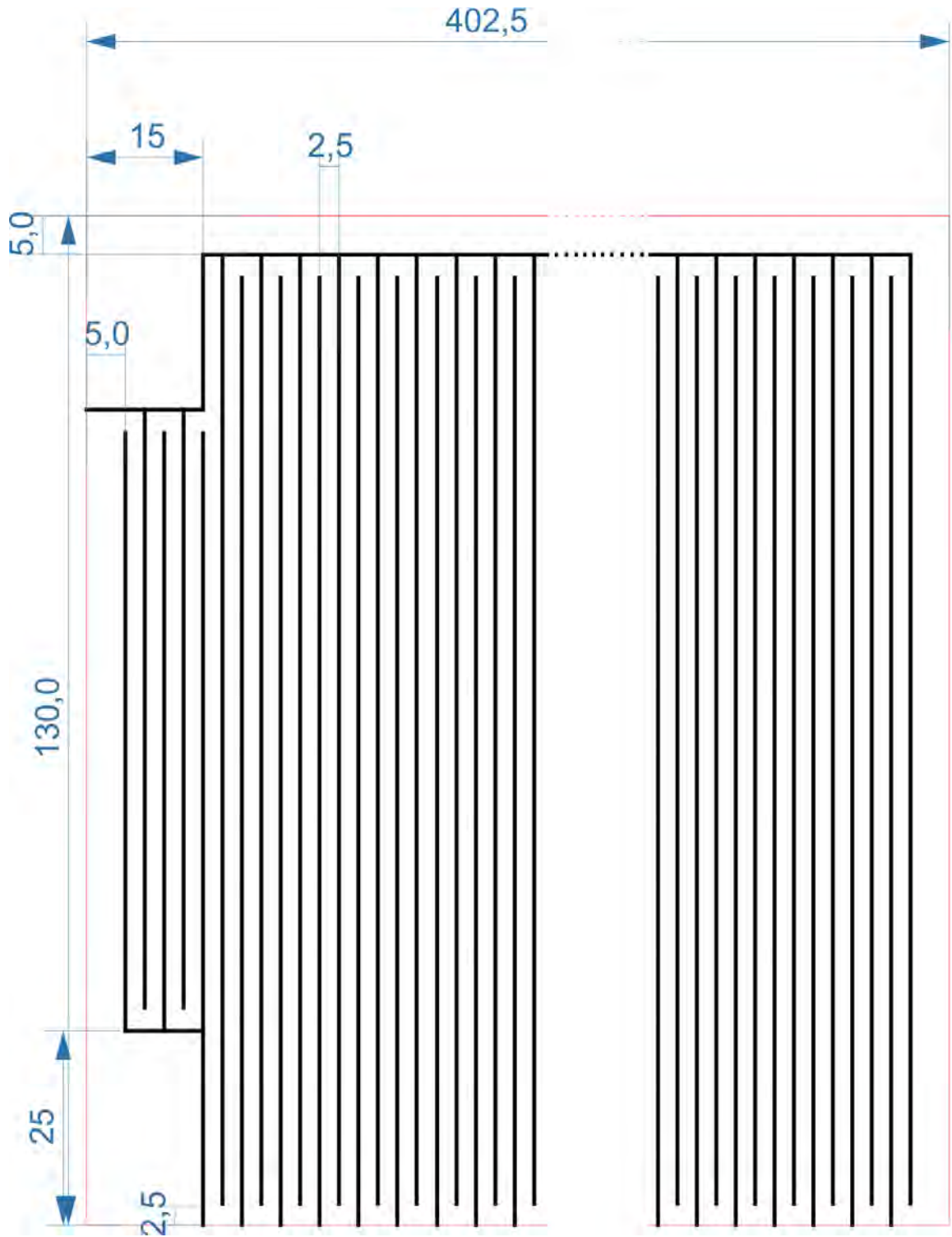


Figure 3.2: Detail of the pattern for the heating foil (4th layer):
 red lines for cutting and black lines for engraving with a linewidth of 0.5 mm.

purchased a laser cutter system (PLS6MW) from Universal Laser Systems[®], with two changeable lasers. The two lasers available are:

- CO₂-laser with a wavelength of 9.3 μm and a maximum laser power of 50W
- fibre-laser with a wavelength of 1.06 μm and a maximum laser power of 40W

Initial test showed that the fibre-laser is much more suitable to treat the aluminium. This is plausible looking at the absorption spectrum of aluminium [6], which is shown in Fig. 3.3. While the absorption-coefficient of aluminium for $\lambda = 9.3 \mu\text{m}$ is almost zero it

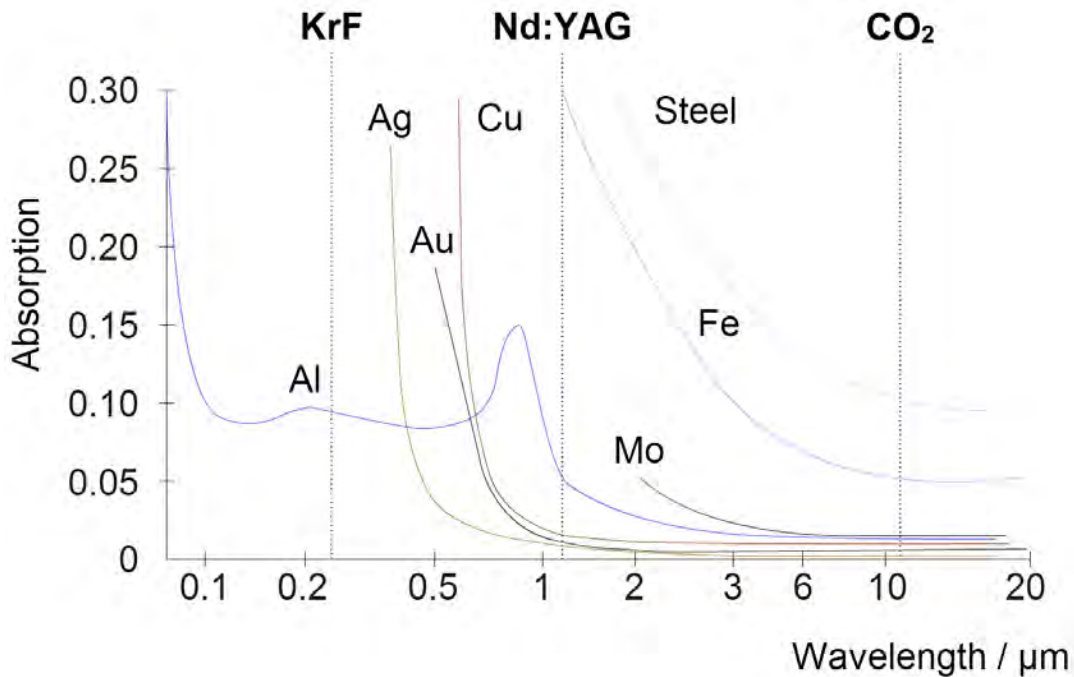


Figure 3.3: Absorption spectrum of aluminium and other metals.

is about 5% for $\lambda = 1.06 \mu\text{m}$. The laser platform consists of a cutting table, which can be moved up or down to adjust the focus to the sample, a 2D movable head directing the laser to the sample, an inlet for pressured air (or gas) directed to the cutting point, a powerful smoke extractor system, several safety precautions and a docking head for the lasers. With the included software, several parameters can be adjusted:

- movement speed of the head
- height of the table (and therefore the height of the focus relative to the sample)
- power of the laser

- frequency of the pulses
- density, definition and contrast (raster-mode only)
- waveform (fibre-laser only)

The results of the cutting resp. rastering strongly depends on the choice of values for the parameters. Fig. 3.4 shows a test pattern to determine the best settings for the raster-mode. Black areas are not necessarily burned Kapton[®], but can also be burned glue, with which the aluminium is laminated to the Kapton[®]. Small and thin remnants of aluminium can be removed by scratching it off with a fine needle. Besides one can observe, that the “/” direction, which is the primary moving direction of the head, is treated better than the “\” direction. The values in Tab. 3.1 yield best results for



Figure 3.4: Tuning-pattern to adjust working parameters of the laser system

25 μm aluminium foil on Kapton[®]. Unfortunately, the value for the height of the focus

	power [%]	speed [%]	freq. [kHz]	z [mm]	contrast	definition	density
cut	100	[5;15]	30	[5;6]	-	-	-
raster	100	[15;35]	30	[5;6]	20	10	80

Table 3.1: Settings used to cut or raster the 25 μm aluminium on Kapton[®]-foil

is not constant, but depends on the position of the head and differs from day to day⁴. Depending on how much the focus is varying over the table, different speeds are needed to achieve satisfying results. E.g. if the focus is more varying over the table on one day

⁴Maybe the system has to be recalibrated.

the speed should be lowered, so that more aluminium can evaporate. This may cause damage to the Kapton[®] in areas in which the focus is well tuned, which eventually has to be repaired with Kapton[®]-tape.

The processing of the foil with the pattern in Fig. 3.2 takes three to four hours. After that the foil has to be scratched manually to remove small remaining aluminium “jumpers” (see Fig. 3.5a). Otherwise, the resistance would be lower (about three to five ohms) and the heating would be more uneven. The resistances of the final foils, and the necessary currents and voltages are given in Tab. 3.2. The values in Tab. 3.2 are just rough clues,

		100 mW/cm ²			150 mW/cm ²	
		R	I	V	I	V
		[Ω]	[A]	[V]	[A]	[V]
4 th layer	1	13.8	1.94	26.79	2.38	32.81
	2	13.7	1.95	26.79	2.39	32.69
	3	13.5	1.96	26.50	2.40	32.45
	4	13.0	2.00	26.50	2.45	31.84
3 rd layer	1	12.1	1.91	23.07	2.34	28.26
	2	12.0	1.91	22.98	2.35	28.14
	3	12.0	1.91	22.98	2.35	28.14
	4	11.9	1.92	22.88	2.36	28.03

Table 3.2: Resistances of the foils at 20 °C. Foils are numbered anticlockwise, looking in z-direction (against air flow).

since the resistances changes with the temperature. Nevertheless the aim to reduce the current by choosing a higher resistance is obtained. Unfortunately the resistances of the 4th layer foils are slightly to big to achieve the 150 mW/cm² powering with one HAMEG HMP 4040, so that three of them are needed overall⁵.

One of the final foils is shown in Fig. 3.5b.

Connections For The Thick Foils

With the intention to stay within the “thin foil concept” different alternatives for connecting the foil were tested. Since the thicker foil is much more robust, less attention has to be paid on the connections. Nevertheless screwable clumps were taken, to err on the side of caution (Fig. 3.6). Besides they can be fixed to a frame, making the design mechanically more stable.

⁵Luckily three are available.



(a) Remnants of aluminium (marked in red).



(b) Heating pattern on foil ready for usage.

Figure 3.5: Results of the laser and manual processing

3.1.3 Support Structure

To arrange the foils in two concentric cylinders and position them in the center of the flow reactor a support structure is needed. It consists of a cage-like frame, where the foils are glued on, two end-rings which hold this framework centrally inside the flow reactor and two additional frames mounted to the rings, supporting the connectors.

3D Printed Framework

As mentioned before a “thin foil model” already existed before this thesis. The foils of this model are glued on a 3D printed framework, designed and printed by the development and construction department of the PI workshop. Although the “thin foil model” wasn’t workable, we didn’t want to destroy it in order to get the framework and therefore another frame was printed. Fig. 3.7 shows the framework with three foils of



Figure 3.6: On the right: Connector mounted to a heating foil.
On the left: Prepared holes for the screws.

the 3rd layer already glued on.

End-Rings

The end-rings are machined from aluminium and are supposed to hold the printed framework and position it in the flow reactor. Therefore the framework can be screwed to the rings. The outer radii of the rings are slightly smaller than the inner radius of the flow reactor, such that the model keeps its position in the reactor and still can easily be pulled in and out. The rings are however naturally well electro- and thermo-conductive, which makes it more difficult to electrically separate the foils from each other and the rings will carry away heat from the foils, which distorts the measurements. The former issue could be solved with relatively little effort by using Kapton[®]-tape as insulator between rings and foils. The later issue could not be prevented and therefore has to be considered in the analysis of the measurements.

Connector Support Frame

The two support structures for the connectors were cut out of wood with the laser⁶. Each is assembled from two plain rings and one pattern, based on the aluminium rings. The structure is then glued on the aluminium end-rings, as shown in Fig. 3.8.

3.1.4 Assembling Of The Model

The heatable foils are scaled such that they tightly fit between the braces of the framework and the end-rings, to utilize as much space as possible and not leaving too much unused space. Both layers are supposed to be glued onto the framework such that the framework lies below the foils, which makes the gluing process quite tricky. If the outer

⁶The CO₂ laser is the better choice here.



Figure 3.7: Foil supporting framework with three foils glued on.

foils are glued first, it is easy to reach the inside of the inner foils though it then is difficult to fix the inner foils as long as the glue is hardening. Starting with the inner foil it is hard to reach between the inner and the outer foil to dispense the glue. We decided to start with the inner foils, so that we could be sure they are well positioned on the framework. For the outer foils we started on one long edge, reaching inside from the side. As soon as this edge is fixed we went to the other edge in two steps of rolling on the cylinder and glueing along the length of the foil. A UHU® “plus endfest 300TM”⁷ was used and hardened in an oven for about one hour at 60°C. Temperature sensors were glued on one of the inner foils before the corresponding outer foil was glued, which can be seen in Fig. 3.9. After the glueing process the end-rings with the connector support structure were mounted, the aluminium frames were isolated from the foil and the

⁷A two component epoxy resin adhesive.



Figure 3.8: Aluminium end-rings with connector support structure.

connectors were glued to their support structure with instant glue⁸. Then the eight temperature sensors for the outer layer were mounted temporarily and fixed⁹ to the foil straight above the foil with the inner sensors. After some test measurements made in order to decide if this particular foil is heating evenly the sensors were fixed permanently to the foil with thermally conductive adhesive.

⁸Instant glue is easy to use and not permanent, in case one wants to disassemble the end-rings from the foils.

⁹With thermally conductive grease.



Figure 3.9: Four temperature sensors positioned on one of the inner foils. The glueing process is nearly completed.

3.2 Temperature Data Acquisition

In order to monitor and record the temperatures on the surface of the model, twelve temperature sensors are glued onto the foils, eight of them aligned on one of the outer foils and four on the foil directly below that one. Both sets are distributed with roughly the same distance between each other on a straight line parallel to the axis of the model (see Fig. 3.9 and Fig. 3.10). The sensors used in the setup are Pt1000 resistance thermometers. All are soldered to wires, which lead out of the flow reactor¹⁰. Outside the reactor they are connected to LEMO cables, which are plugged into current sources¹¹. The box, carrying the sources has additional plugs to connect the ADC¹² channels of a LogicBox DL706¹³ via a flat ribbon cable. The ADC channels are used differentially. The LogicBox is connected to a PC via USB, where the data is handled by a LabVIEW[®]

¹⁰The cables of the inner sensors are interrupted by a connector, glued on the framework, so that they can be plugged and unplugged.

¹¹Constant 1 mA and a maximum of about 20 V.

¹²Analog to Digital Converter.

¹³A multifunctional device build by the electronics workshop of the PI.

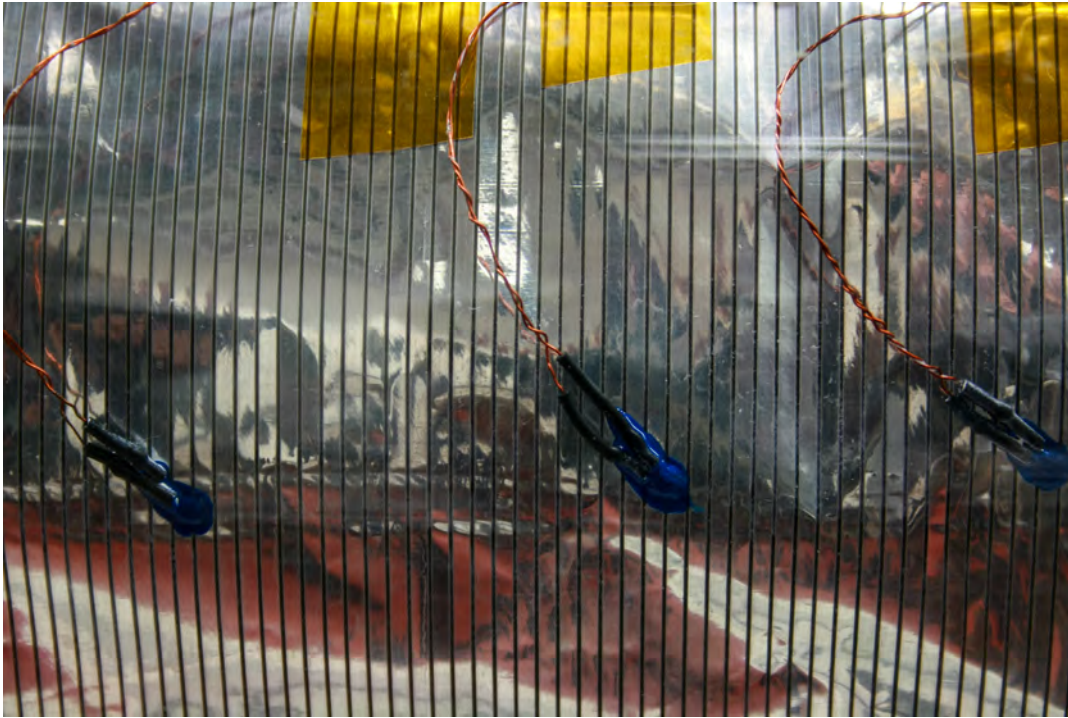


Figure 3.10: Temperature sensors glued on an outer foil with thermally conductive glue.

program. In the following, the functional principle of resistance thermometer will be explained and the LabVIEW[®] program will be described.

3.2.1 Resistance Thermometer

In general the electrical resistivity of most materials is dependent on the temperature. Although in some cases this is inconvenient, it can be used to determine the temperature. Today resistance thermometers are a fairly established form of thermometers. Due to the practical attributes of platinum, sensors made from platinum are most common among those and are abbreviated with PtXXX, where XXX stands for the resistance measured in Ohm at 0 °C, e.g. Pt100 with 100 Ω at 0 °C. To ensure reproducibility of the Pt-sensors, their characteristics are specified in norms IEC 751 (international) and DIN EN 60 751 (German). According to these norms, the resistance R of a Pt-sensor

has to depend on the temperature T (measured in $^{\circ}\text{C}$) following the polynomials [7] :

$$R(T) = R_0 (1 + A \cdot T + B \cdot T^2 + C (T - 100^{\circ}\text{C}) \cdot T^3) \quad T \in [-200^{\circ}\text{C}; 0^{\circ}\text{C}] \quad (3.16)$$

$$R(T) = R_0 (1 + A \cdot T + B \cdot T^2) \quad T \in [0^{\circ}\text{C}; 850^{\circ}\text{C}] \quad (3.17)$$

The parameters A , B and C are equal for all types of Pt-sensors and given by:

$$A = 3.9083 \cdot 10^{-3} \text{ }^{\circ}\text{C}^{-1}$$

$$B = -5.775 \cdot 10^{-7} \text{ }^{\circ}\text{C}^{-2}$$

$$C = -4.183 \cdot 10^{-12} \text{ }^{\circ}\text{C}^{-4}$$

while the value for R_0 is the resistance at 0°C and therefore defines the different Pt-sensors. The IEC and DIN norms categorize the Pt-sensors in classes, which define the tolerances of the sensors. The sensors used for this setup are Pt1000 from Labfacility[®] of the IEC 751 class B [8]. The temperature measurement inaccuracy of class B sensors is defined by:

$$\Delta T = \pm (0.30 + 0.005 \cdot |T|) \quad (3.18)$$

and is valid for the full temperature range from -200°C to 850°C . Since the setup runs with air at room-temperature and heats up, Eq. (3.17) is used in the following. To determine the temperature T from the measured resistance R , Eq. (3.17) has to be converted:

$$T(R) = \frac{-AR_0 \pm \sqrt{A^2R_0^2 - 4BR_0(R_0 - R)}}{2BR_0} \quad (3.19)$$

where of course the “+” term applies¹⁴. According to [7], Eq. (3.19) can be approximated linearly with:

$$T(R) = \frac{R - R_0}{R_0 \cdot \alpha} \quad \text{with} \quad \alpha = 3.85 \cdot 10^{-3} \text{ } ^\circ\text{C}^{-1} \quad (3.20)$$

$$\Leftrightarrow R(T) = R_0 (1 + \alpha \cdot T) \quad (3.21)$$

The comparison of Eq. (3.19) and Eq. (3.20) reveals that the difference of both approximations is negligible in the temperature domain from 20 °C to 100 °C, which is visualized in Fig. 3.11. The plotted error domains derive from Eq. (3.18) . Furthermore, the Pt1000

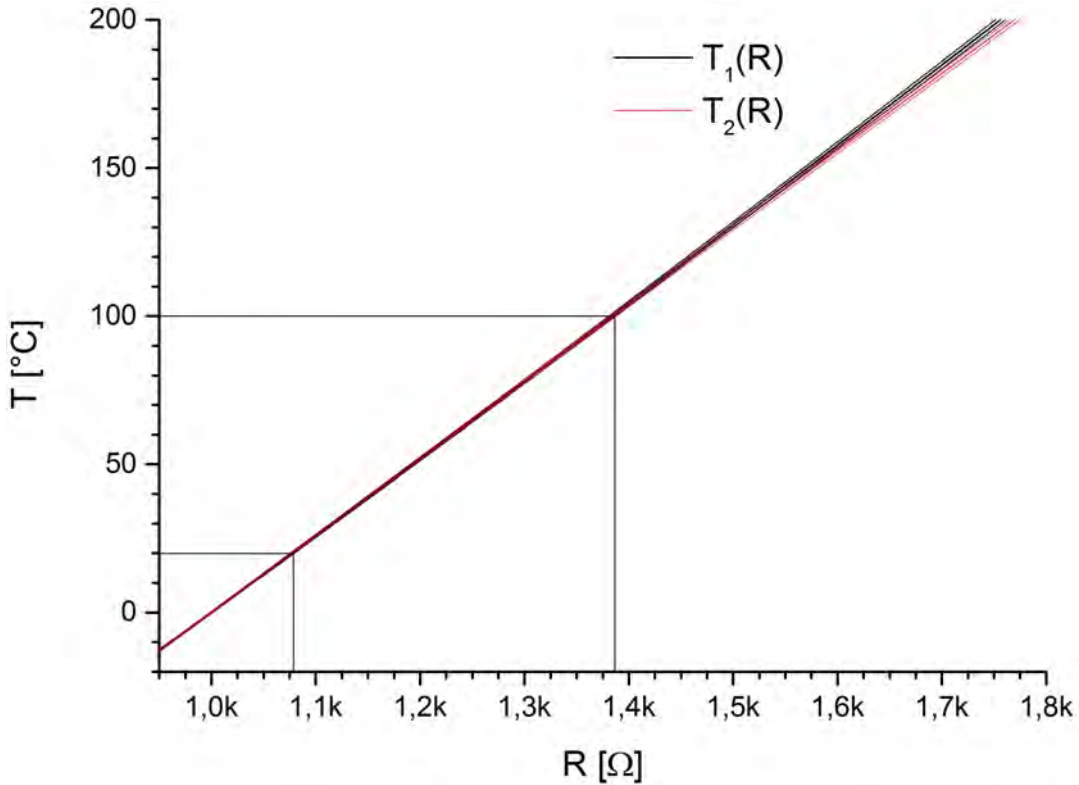


Figure 3.11: Comparison of the exact IEC/DIN formula (3.19) : $T_1(R)$ and the linear approximation (3.20) : $T_2(R)$.

are soldered to thin copper wires ($\varnothing \approx 0.1 \text{ mm}$) to install them on the model, so that the additional resistance of the wires and the solder joints might compromise the temperature measurements. Therefore a recalibration of the sensors was made, which is described in section 4.1.1.

¹⁴The “−” term is the solution of the function (3.17) for extremely high temperatures, where the function is no longer applicable.

To measure the resistance R of a resistor a voltage has to be applied so that a current flows. Knowing both, current I and voltage U one can use the definition:

$$R = \frac{U}{I} \quad (3.22)$$

Obviously it is reasonable to define either of them and measure the other. Because the measurements are carried out with an ADC, which senses voltages, the Pt1000 are connected to a constant current source while the voltage is measured. Since the used ADC channels are sensitive for voltages from 0 V to 2.5 V [9], currents of 1 mA are applied to the Pt1000, so that the resistance R is translated into voltage V by:

$$R[\text{k}\Omega] \longrightarrow U[\text{V}] = R \cdot I = \frac{R}{\text{k}\Omega} \cdot 1 \text{ mA k}\Omega = \frac{R}{\text{k}\Omega} \text{ V} \quad (3.23)$$

Thus resistances between 0 k Ω and 2.5 k Ω can be measured, which is more than enough to cover the temperature interval of interest.

As a consequence of the resistance measurement, a current of 1 mA runs through the sensors. Hence they consume power, which is given by Eq. (3.15). For a resistance about 1.4 k Ω (reached at about 100 $^{\circ}\text{C}$) the power consumption is about 1.4 mW. Calculated for the surface of the sensor this is less than 5 mW/cm 2 and therefore small compared with the power consumption of the foils (150 mW/cm 2). A Pt100 sensor on the other hand would have to be powered with 10 mA to obtain the same temperature range and since the power increases with the square of the current it would heat with 14 mW, or about 50 mW/cm 2 , for a sensor of the same size. The IEC and DIN norms imply a self heating parameter E , which has to be specified in the sensor's datasheet [7] and is defined by:

$$E = \frac{\Delta T}{R \cdot I^2} \quad (3.24)$$

where ΔT is the additional temperature caused by the power consumption given by the measurement-current I and the resistance R , while the sensor is positioned in an air flow of 2 m/s, which is about the minimum air speed used in our measurements. For high temperatures of 100 $^{\circ}\text{C}$ and a current of 1 mA and a self heating parameter of $E < 0.5 \text{ }^{\circ}\text{C}/\text{mW}$ [8] a temperature-difference of $\Delta T < 0.7 \text{ }^{\circ}\text{C}$ is obtained. This is a systematic error that has to be taken into account.

3.2.2 LabVIEW Program

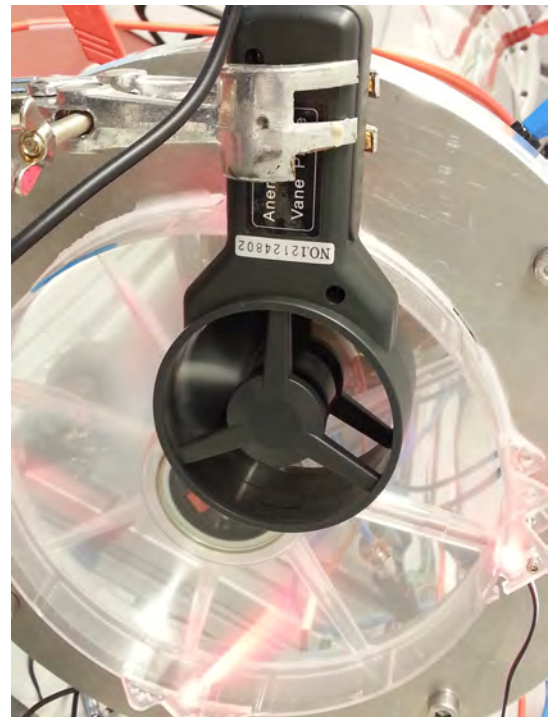
To collect and process the voltages measured by the ADC a LabVIEW® program was created. It fetches the voltages of the eight differential channels of the LogicBox ADC. In order to reduce the noise caused by the ADC in the data, each measurement-point is obtained by averaging over 10 measurements of the ADC. With the resulting voltage values and the calibrations parameters (see section 4.1.1 and Tab. 4.1) the temperature is calculated giving one measurement point. The temperatures for all sensors are obtained shortly after each other. After a few seconds the next sequence of temperatures are taken. The change of temperatures is displayed for monitoring, so that one can determine if the thermal equilibrium is reached and a measurement can then be started. Furthermore the current temperature profile is plotted. All temperatures are written into a file with a time-stamp for later analysis. Additionally the air speed and room temperature, the heating power, the position of the measured foil and more additional informations are saved in these files.

3.3 Flow Reactor

To provide a constant and uniform air flow, the model is positioned in a flow reactor (see Fig. 3.1). It consists of a tube made from acrylic glass with an inner diameter of about 220 mm and has a wall thickness of about 10 mm. On both ends, flanges are mounted, on which fans can be screwed. This provides a solid mounting for the fans and gives the opportunity to access the inside of the reactor. Including the flanges and fans the reactor has a length of about 1.05 m. To supply the model with power, two times eight holes were drilled into the acrylic glass at about $1/4$ and $3/4$ of the length. Into these holes connectors for banana plugs are mounted, which on the inside are connected to cables, which in turn can be plugged to the connectors of the heating foils. The fans mounted to both sides of the reactor blow in the same direction to achieve a more uniform flow than a single fan could provide. They are commercial PC fans and should, according to their datasheet be powered with 12 V, however they endure voltages up to at least 23 V which were used during measurements to obtain higher air flows. The air speed is measured with an anemometer from PeakTech®, directly in front of the fan on the advection side (see Fig. 3.12b). The anemometer simultaneously measures the temperature of the inflowing air.



(a) The display of the anemometer with airspeed and temperature values.



(b) The measure-fan of the anemometer with inbuilt thermometer.

Figure 3.12: The anemometer.

4 Measurements

In order to investigate the cooling of the model, several measurements were performed. The temperature was taken on one of the surfaces representing the 4th layer at eight points and on one of the foils representing the 3rd layer at 4 points, both sets aligned parallel to the cylinder's axis. The measurements were taken at 100 mW/cm² and at 150 mW/cm². For both power consumptions, the air speed was varied from a maximum of about 3.8 m/s down until the temperature reached values of about 100 °C, in order to not destroy the model. All these measurements were taken at three different positions in φ (cylindric coordinates) at 0° (upside), 90° (side) and 180° (downside). Additionally a measurement without any air flow was carefully performed at very low power¹.

For all settings, the thermal equilibrium of the model was awaited and then the temperatures of all Pt1000 were captured 100 times (each of these 100 measurements already consist of 10 data points of the ADC, which are averaged), distributed over a time of about 15 minutes. During the measurements, the room/air temperature and the air speed were recorded. The measurements I will present in the following display the temperature difference ΔT between the temperature of the model and the room temperature², because the absolute temperature naturally depends on the temperature of the air which is flowing in. If an air flow is applied it is always directed against the z-axis, so that the air reaches the model at $z = 400$ mm first and then flows to the other end of the model (at $z = 0$). Before meaningful measurements could be performed, the temperature sensors had to be calibrated.

In the following necessary auxiliary measurements such as the calibration of the sensors and the air speed measurement and the main measurements will be described.

¹Again in order to not destroy the model.

²Since the room temperature always was about 20 °C, one can roughly estimate the absolute temperature by adding 20 °C.

4.1 Auxiliary Measurements

4.1.1 Calibration

As discussed before, the Pt1000 themselves have fairly small inaccuracies, but are attached to different parts, which all constitute sources of errors, e.g. the wires and solder joints have additional resistances ($\approx 2\ \Omega$ were measured for one of the wires), the inaccuracies of the current sources and the voltage measurement. The additional resistances seemed to be the main origin of errors among them. With a calibration, including all parts of the readout system, the systematic errors should be minimized. The first attempts were made by thermalizing the sensors³ in ice water, measure the resistance with the setup and the temperature with an accurate reference thermometer, then raise the temperature to the boiling point, while resistance and reference temperature are recorded. Not too surprisingly, the results were not satisfying, as the response time of the tiny sensors is shorter than the one of the reference thermometer. The Pt1000 measures therefore the temperature before the reference temperature.

Therefore a calibration, for which the thermal equilibrium is awaited, should give much better results. This was performed by placing the sensors and the reference thermometer in an oven, setting a temperature and waiting until the displayed temperature of the reference thermometer was fairly constant. The air inside the oven was circulated with a fan, so that the selfheating of the sensors should be roughly similar in the oven and in the flow reactor. The resistances and the reference temperature then were measured for about 15 min resp. 100 measurements, as before every single one of the 100 measurements is already the average over 10 measurements of the ADC. This was repeated for temperatures from 20 °C to 100 °C in steps of 10 °C. The average of the resistance and the standard deviation for every single sensor then were plotted against the reference temperature and their standard deviation. The data were fitted with a linear fit and for comparison with a polynomial of second order (see section Resistance Thermometer 3.2.1 : Eq. (3.17) and Eq. (3.21)). Fig. 4.1 shows exemplary fits for the sensor connected to channel 0 of the LogicBox. As expected, the difference between the linear and the polynomial fit is marginal ($< 0.15\ \text{°C}$ over the full range) and therefore the linear fit was used in the following. The linear fit is of the form:

$$R = R_0 + \beta \cdot T = R_0 + (R_0 \cdot \alpha) \cdot T \quad (4.1)$$

³Of course only the sensors, before they were glued to the foils.

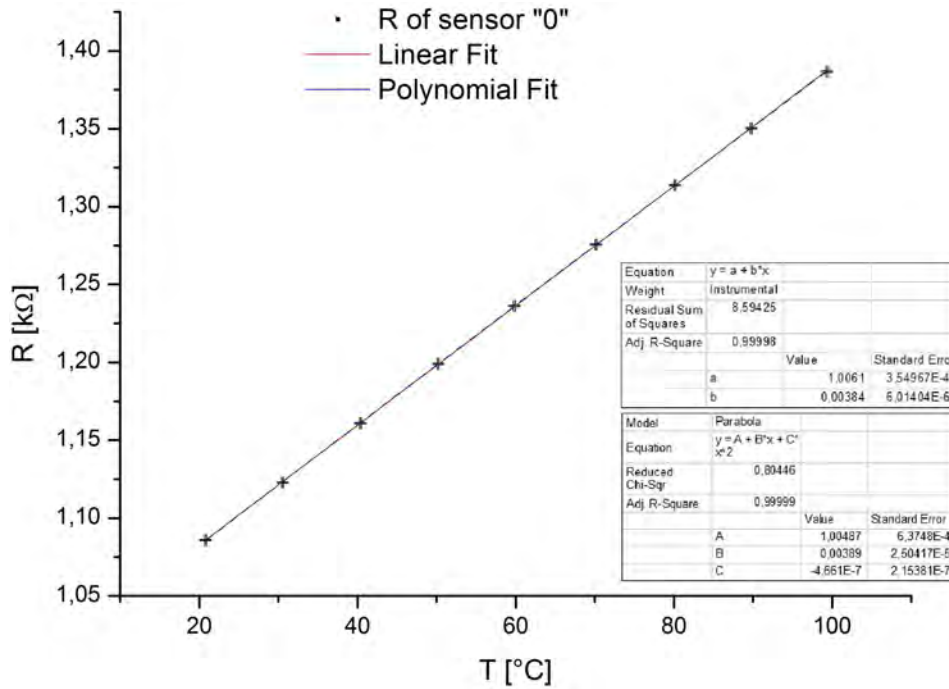


Figure 4.1: Calibration of sensor “0”.

where α is the parameter in Eq. (3.20) and β is the parameter used by Origin[®] for the fitting function. The calibration parameters found with the fits are listed in Tab. 4.1.

Apparently the calculated zero-crossing resistances R_0 have systematic offsets of several ohms (from about 4Ω to about 12Ω), which mostly come from the wires and solder joints, but may also partly arise from the current sources, if they provide slightly too much current, or the ADC, if they measure a slightly higher voltage than applied. Furthermore the slope parameter α is up to 1% smaller than given by the IEC/DIN norms, so that the resistance rises a bit slower with the temperature than expected, which makes sense since parts of the additional resistances are outside the heated area and therefore do not rise with the temperature inside. Since the calibration was performed for the full operating range of temperatures and with all parts of the readout system included, systematic errors should mainly be compensated.

4.1.2 Air Speed

Since the measured air speeds fluctuated fairly much, the supply voltages for the fans were adjusted and varied in fixed steps instead of trying to control the air speed to fixed values. The air speed was observed and entered in the LabVIEW[®] program manually during the measurements and then averaged. Fig. 4.2 shows an example for the air speed

Calibration Parameters

	name	z [mm]	R_0 [Ω]	ΔR_0 [Ω]	β [$\Omega/^\circ\text{C}$]	$\Delta\beta$ [$\Omega/^\circ\text{C}$]	α [$10^{-3}/^\circ\text{C}$]	$\Delta\alpha$ [$10^{-3}/^\circ\text{C}$]
4^{th} Layer	0	25	1,006.10	0.40	3.84	0.01	3.82	0.01
	1	65	1,007.11	0.32	3.84	0.01	3.81	0.01
	2	115	1,004.37	0.22	3.83	0.01	3.81	0.01
	3	180	1,005.79	0.18	3.84	0.01	3.82	0.01
	4	235	1,007.11	0.30	3.83	0.01	3.80	0.01
	5	280	1,006.89	0.28	3.85	0.01	3.82	0.01
	6	325	1,011.84	1.44	3.83	0.03	3.79	0.03
	7	380	1,007.80	0.60	3.85	0.01	3.82	0.01
3^{rd} Layer	0	50	1,007.73	0.57	3.87	0.01	3.84	0.01
	1	150	1,004.94	0.60	3.85	0.01	3.83	0.01
	2	250	1,006.81	0.57	3.87	0.01	3.84	0.01
	3	350	1,006.42	0.59	3.88	0.01	3.86	0.01

Table 4.1: Calibration parameters for the Pt1000 sensors.

data. Because the data were recorded manually and the fluctuations were quite fast, the error of the air speed was rounded up to 0.1 m/s. Additionally the anemometer was fairly sensitive to variation of the angle and position relative to the fan. Whenever the anemometer had to be removed, we tried to always find the position where the measured speed was maximal, in order to obtain reproducible results.

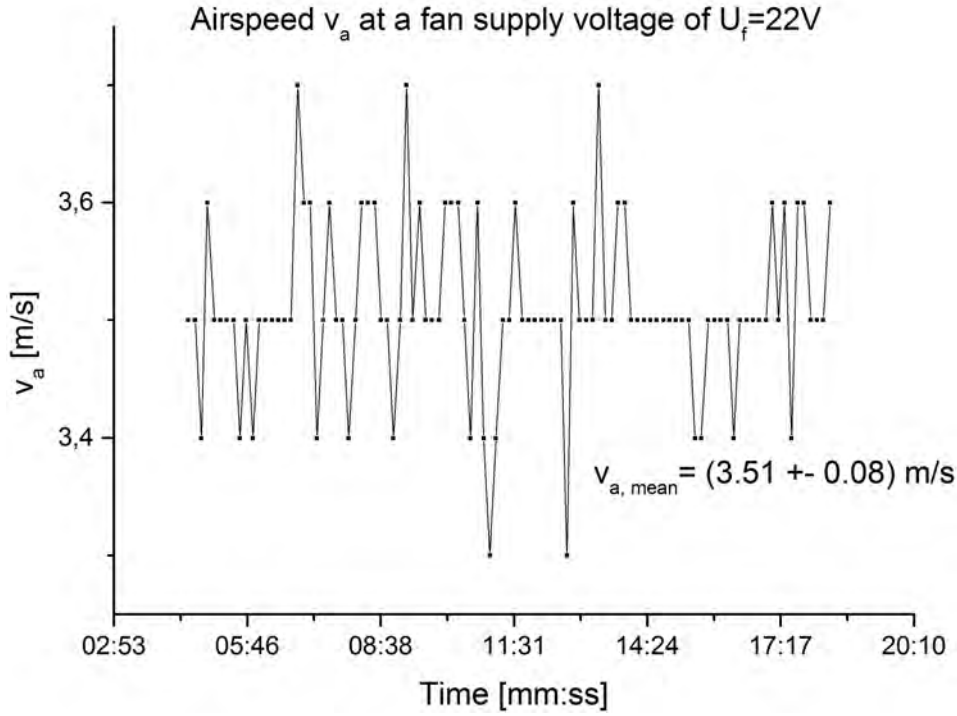


Figure 4.2: Air speed fluctuations.

4.2 Main Measurements

4.2.1 Measurements Without Air Flow

To demonstrate how important an active cooling is for the detector, the model was heated without an applied air flow. This was done at very low powers (10 mW/cm^2 , 20 mW/cm^2 and 30 mW/cm^2 - see Tab. 4.2), since the model already approached temperatures, which might be dangerous for it. The temperature-profile (at thermal equilibrium) for the different

P/A [mW/cm ²]	P/F 3 rd layer [W]	$\sum P$ 3 rd layer [W]	P/F 4 th layer [W]	$\sum P$ 4 th layer [W]	$\sum P$ [W]
10	4.40(1)	17.60(2)	5.20(1)	20.80(2)	32.40(3)
20	8.80(1)	35.20(2)	10.40(1)	41.60(2)	76.80(3)
30	13.20(1)	52.80(2)	15.60(1)	62.40(2)	115.20(3)

Table 4.2: Powers used for the measurements without air flow. P/F is the power per foil.

powers is shown in Fig. 4.3.

As one can see, the profiles are fairly flat, but have falling edges on both sides, which might be caused by the end-rings which carry away heat, since they are well thermally

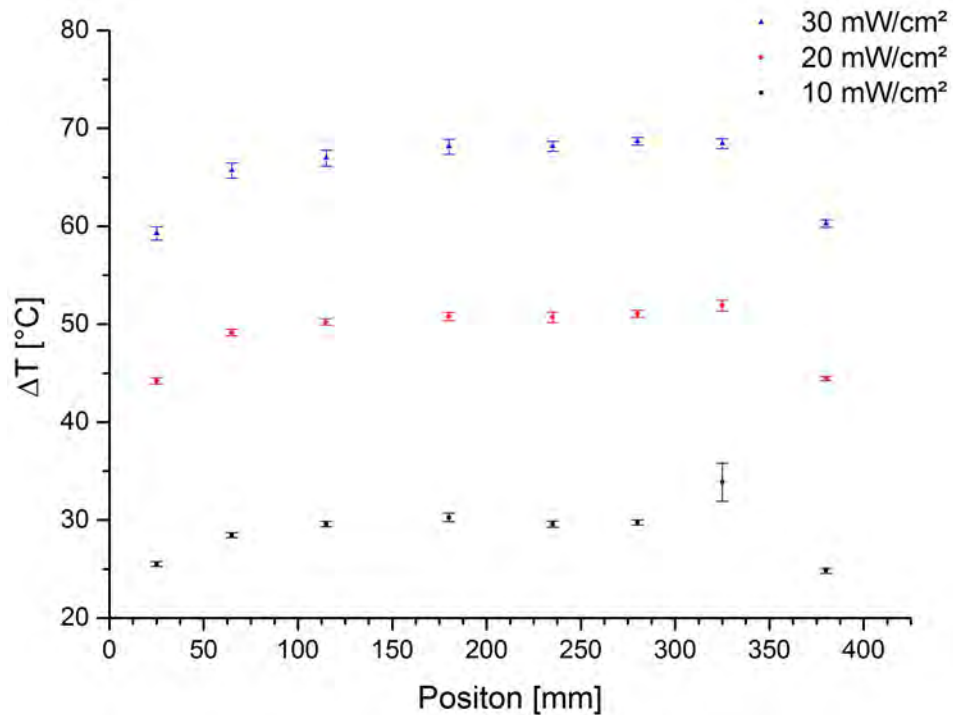


Figure 4.3: Temperature profiles at different powers without air flow.

conductive and have big surfaces and by the fact that the foil has less neighbouring heating foil towards the edges. Nevertheless this is a good indication for the even heating of the foils. Further, one can see that the temperatures already reach about $90\text{ }^{\circ}\text{C}$ (absolute) at powers of 30 mW/cm^2 . To clarify this, the means of the sensors from $z = 65\text{ mm}$ to $z = 280\text{ mm}$ were averaged⁴ and plotted against the power, which can be seen in Fig. 4.4. This measurement of course is just a qualitative verification that the detector really has to be cooled actively, but does not really allow an estimation of radiation cooling of the model, since it is not placed in vacuum or even sealed. Since warm air came out of both sides of the flow reactor during the measurements it was cooled passively via convection. A $T^4 \propto \frac{P}{A}$ behaviour therefore is neither expected nor observable in Fig. 4.4. Convection is an effect that could not occur in a sealed detector. Thus active cooling is absolutely necessary.

⁴Edges were excluded, because of the systematically falling edges and the sensor at $z = 325\text{ mm}$ because of the failure of the measurement at 10 mW/cm^2 .

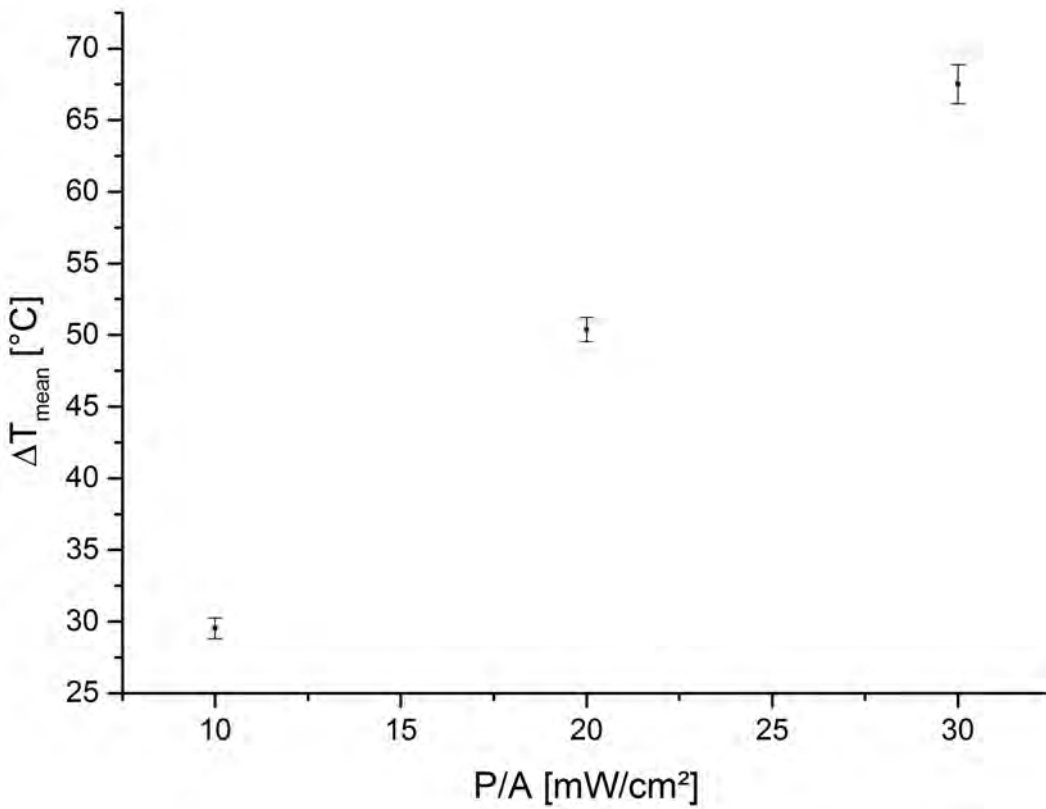


Figure 4.4: The mean temperature at different powers without air flow.

4.2.2 Measurements With Air Flow

As mentioned before, measurements were performed with heating powers of 100 mW/cm² and 150 mW/cm². Tab. 4.3 shows the corresponding powers per foil and total powers. In

P/A [mW/cm ²]	P/F 3 rd layer [W]	∑P 3 rd layer [W]	P/F 4 th layer [W]	∑P 4 th layer [W]	∑P [W]
100	44.00(5)	176.00(10)	52.0.(5)	208.00(10)	324.00(15)
150	66.00(5)	264.00(10)	78.00(10)	312.00(20)	576.00(23)

Table 4.3: Powers used for the measurements with air flow. P/F is the power per foil.

both cases, the power was kept constant by adjusting the voltage. The voltages were adjusted, since the resistance rises with the temperature and for a system with constant voltage, the power decreases with $P = \frac{U^2}{R}$, while for a system with constant current the power would increase with $P = I^2 \cdot R$, leading to even higher temperatures and resistances. The uncertainties of the heating powers came from the manual adjustments of the power during the measurements. Because the 4th layer-foils had to be powered

with two HAMEG HMP 4040 to achieve 150 mW/cm^2 , the uncertainties of the powers is about double the uncertainty of operating with one power supply, since the reading error was bigger due to the two separated displays.

Temperature Profiles

To illustrate the temperature distribution on the model, profiles are helpful. Fig. 4.5 shows the temperature profile on the 4th layer-foil, while powered with 100 mW/cm^2 , at the upside position and cooled with the listed air speeds. As visible, the temperature

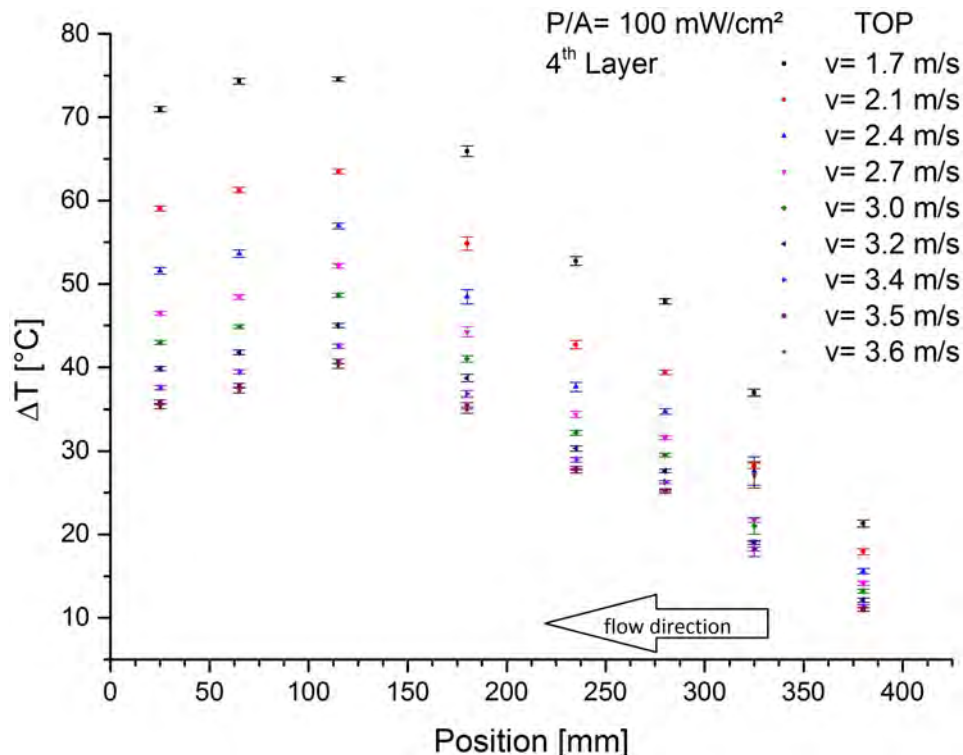


Figure 4.5: Temperature profiles on 4th layer, upside, at 100 mW/cm^2 and different air speeds.

risks roughly linearly towards the hotter end, but then decreases again on the last few centimetres. This should be caused by the heat transport of the end rings ($z_{r1} = 50 \text{ mm}$ and $z_{r2} = 350 \text{ mm}$) and the less neighbouring foil, as discussed before. The same applies for the sensors at the cold end.

Since the HV-MAPS later will more likely heat with 150 mW/cm^2 , the measurements with more power are more important. The temperature profiles on the outer layer for 150 mW/cm^2 , the upside position and different air flows are plotted in Fig. 4.6. It is noticeable that the cooling effect on the hotter edge is stronger than before, which makes

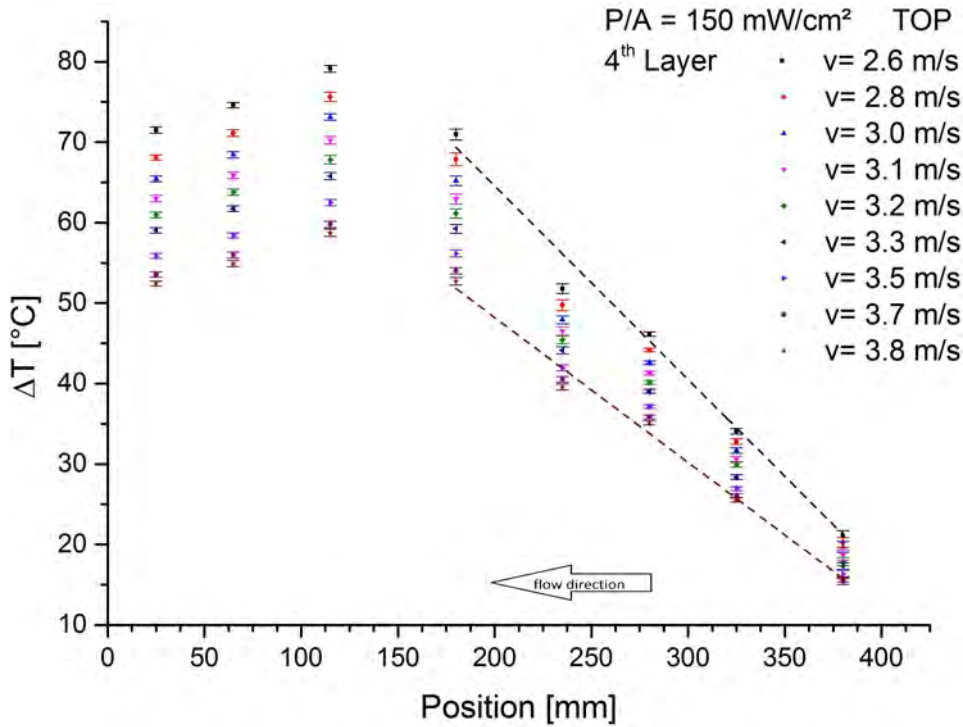


Figure 4.6: Temperature profiles on 4th layer, upside, at 150 mW/cm² and different air speeds and two fits to determine the temperature gradient.

sense considering the “less neighbouring heaters” effect. Together with the cooling end rings, this also explains the slightly lower temperature on the cool edge in comparison to the extrapolation of the slope. Similar to the measurements at 100 mW/cm², the sensor at $z = 235$ mm detects a lower temperature as one would expect looking at the other temperatures. This could be caused by a little bump in the foil which exposes the sensor more to the air flux, or unevenness in the heating of the foil, which eventually can be detected, looking closer at Fig. 4.3. Naturally the temperature rises with decreasing air speed. This also applies for the temperature gradient, since the temperature just before the foils should be at a fixed value of the cooling medium and the temperature right on the edge should be very close to it, but the maximum temperature strongly depends on the flux. To determine the temperature gradient along the z -axis, linear fits were made as it is exemplarily shown in Fig. 4.6. For the two displayed fits, the temperature gradient is about $|\frac{\partial T}{\partial z}| = 0.241(20)^\circ\text{C}/\text{mm}$ (for $v_{air} \approx 2.6$ m/s) and $|\frac{\partial T}{\partial z}| = 0.180(13)^\circ\text{C}/\text{mm}$ (for $v_{air} \approx 3.8$ m/s). More results can be found in the next paragraph.

For the side and bottom position of the measured 4th layer-foil, the temperature profiles are illustrated in Fig. 4.7 and Fig. 4.8.

Both look fairly similar to the the top position profile. This is quite convenient, since

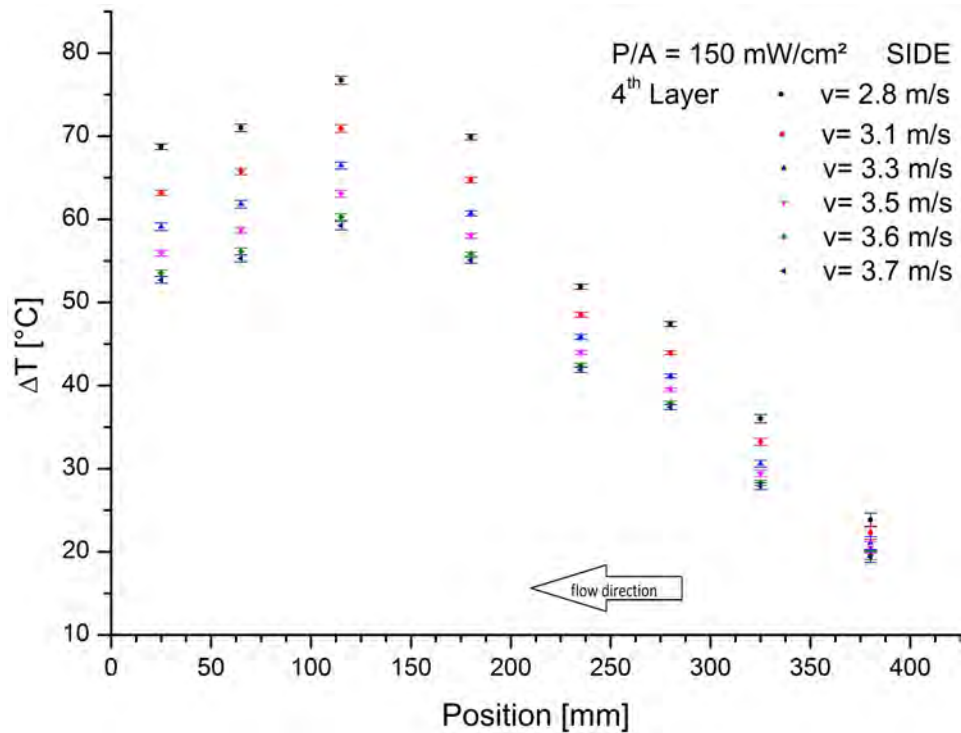


Figure 4.7: Temperature profiles at 150 mW/cm^2 on the side of the 4th layer.

no big gradients in φ direction have to be expected. Though the maximum temperature seems to be lower at the bottom of the model, this is plausible, since the warm air rises upwards along the foils, heating the foils on the side and the top and providing space for cooler air. Furthermore this also effects the temperature gradient at the hotter end of the foil. To have a more direct comparison the profiles for all three positions at $v_{air} = 3.7 \text{ m/s}$ are plotted in Fig. 4.9. The lower maximum temperature for the “bottom”-position is well noticeable.

Equivalent measurements were taken for the 3rd layer foil. One example is illustrated in Fig. 4.10. As visible, the shape of the profile differs significantly from the profiles of the 4th layer. The temperature seems to rise fairly linearly towards the hot end.

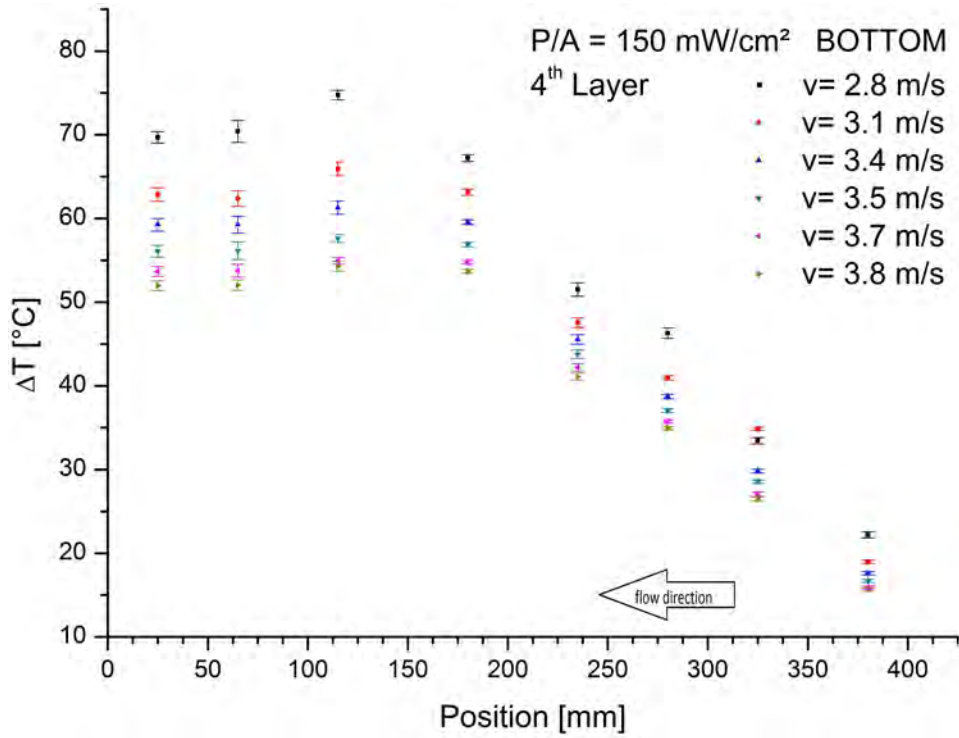


Figure 4.8: Temperature profiles at 150 mW/cm² on the bottom of the 4th layer.

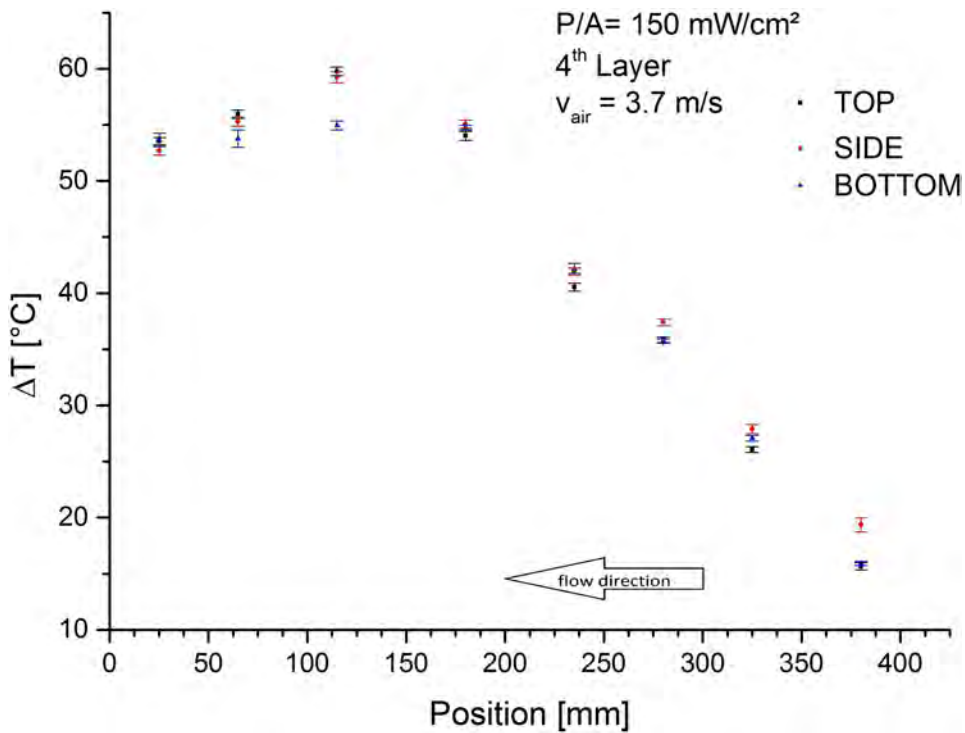


Figure 4.9: Comparison of the profiles for different positions in φ .

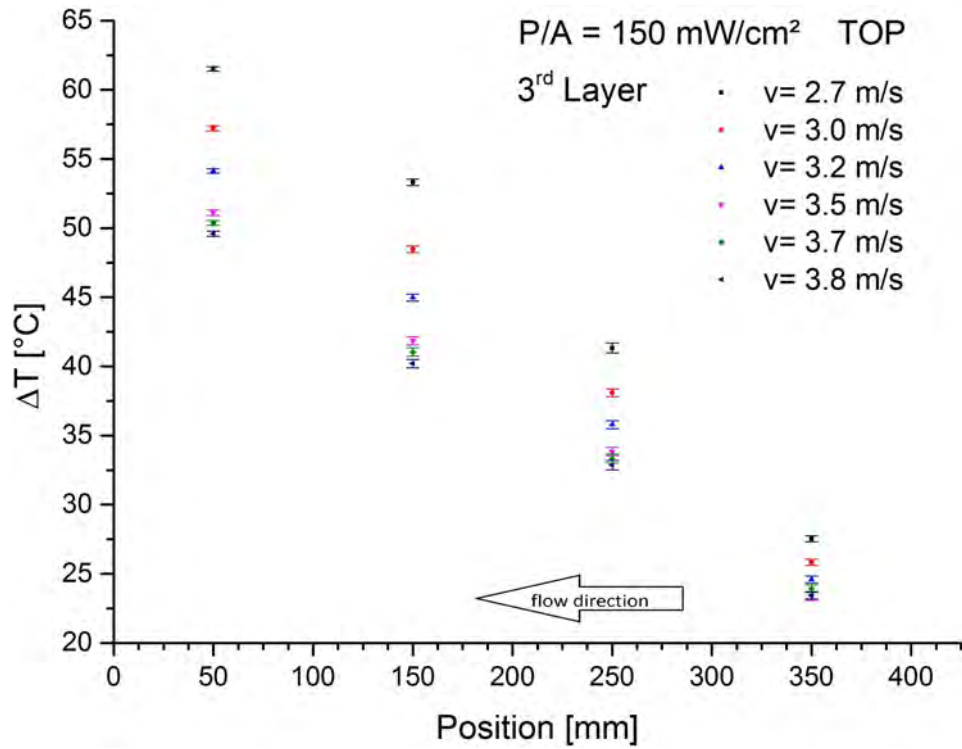


Figure 4.10: Temperature profile on the inner layer at the “top”-position heated with 150 mW/cm² and cooled with different air speeds.

Air Speed Projection

To get a better impression of the flow dependence of the temperature the maximum temperature of the measurements can be plotted against the air speed at constant power consumption of 150 mW/cm^2 . Fig. 4.11 shows this for the top of the 4th layer. For the avail-

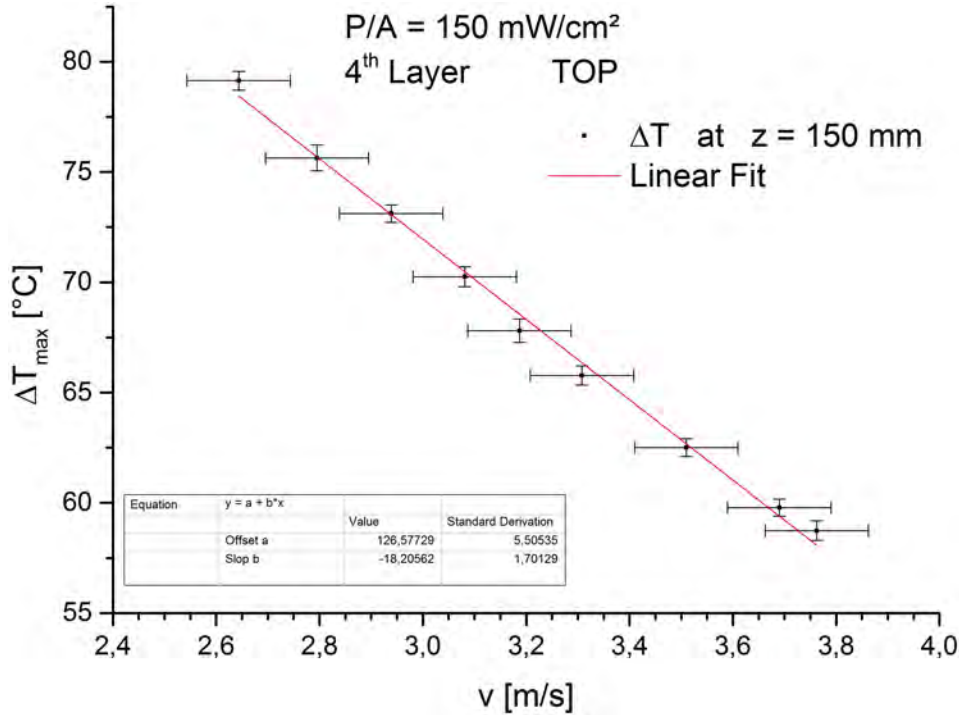


Figure 4.11: Air speed dependence of the maximum temperature on the top of the 4th layer.

able air speed domain, the maximum temperature on the foil seems to decrease roughly linear with the air flow. A linear fit gives a slope $\frac{\partial T}{\partial v}$ of about $\frac{\partial T}{\partial v} = -18.2(1.7) \text{ }^\circ\text{C/m s}^{-1}$. A linear behaviour is not expected theoretically, but the fairly big errors of the air speed prevent better predictions of the behaviour beyond the measured domain. On the side and the bottom of the 4th layer, the behaviour is fairly similar, as Fig. 4.12 and Fig. 4.13 illustrate. The maximum temperature on the side decreases with about $\frac{\partial T}{\partial v} = -18.7(2.4) \text{ }^\circ\text{C/m s}^{-1}$, while the decreasing on the bottom is a bit faster with about $\frac{\partial T}{\partial v} = -21.3(2.7) \text{ }^\circ\text{C/m s}^{-1}$.

As mentioned before, the temperature gradients were determined by applying linear fits on the temperature profiles. For the upside position of the 4th layer-foil the gradients are given in Tab. 4.4 and plotted in Fig. 4.14. The plot reveals that the gradient decreases with the air speed, as it is expected.

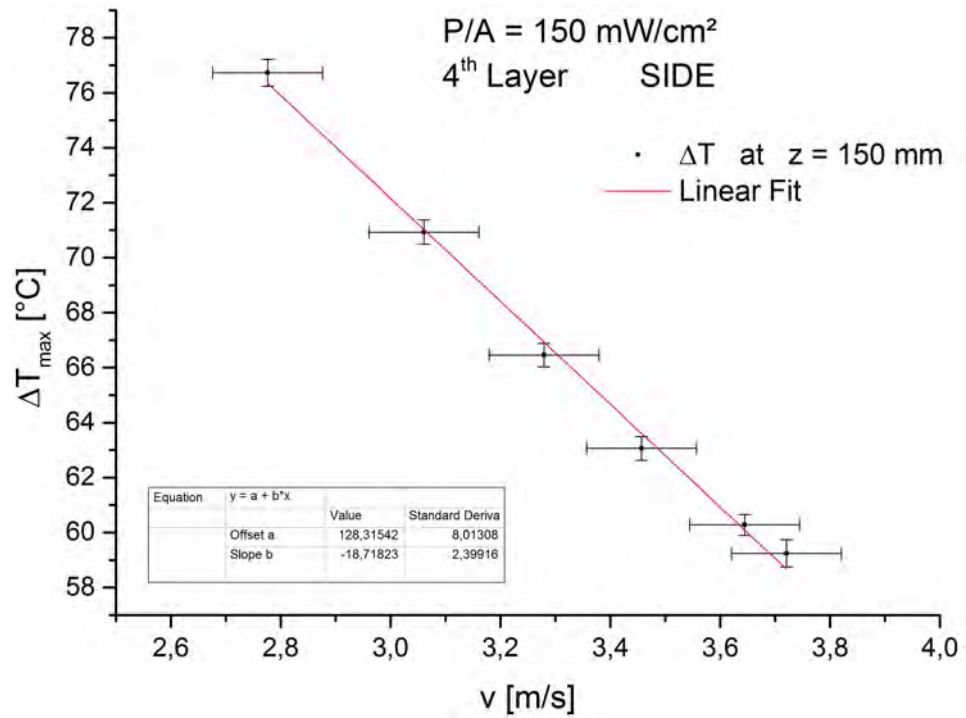


Figure 4.12: Air speed dependence of the maximum temperature on the side of the 4th layer.

$v_{air} \text{ [m/s]}$	2.6	2.8	3.0	3.1	3.2	3.3	3.5	3.7	3.8
$ \frac{\partial T}{\partial z} $	2.41	2.31	2.18	2.12	2.08	2.03	1.93	1.86	1.80
$[\text{°C/cm}]$	± 0.20	± 0.17	± 0.19	± 0.18	± 0.15	± 0.15	± 0.14	± 0.12	± 0.13

Table 4.4: Temperature gradients on the top 4th layer for different air speeds.

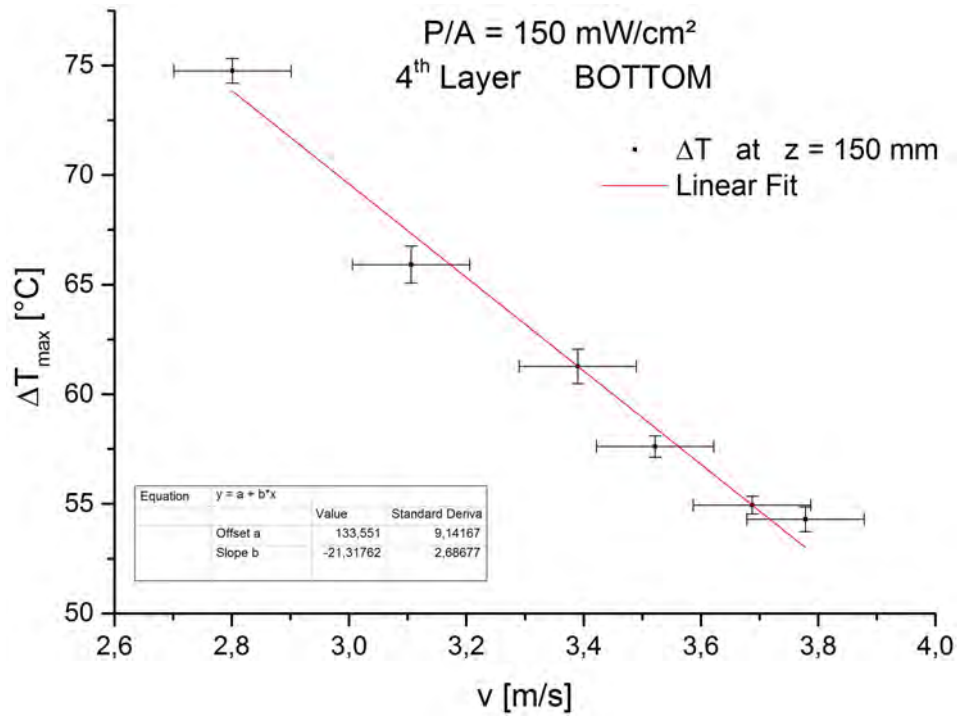


Figure 4.13: Air speed dependence of the maximum temperature on the bottom of the 4th layer.

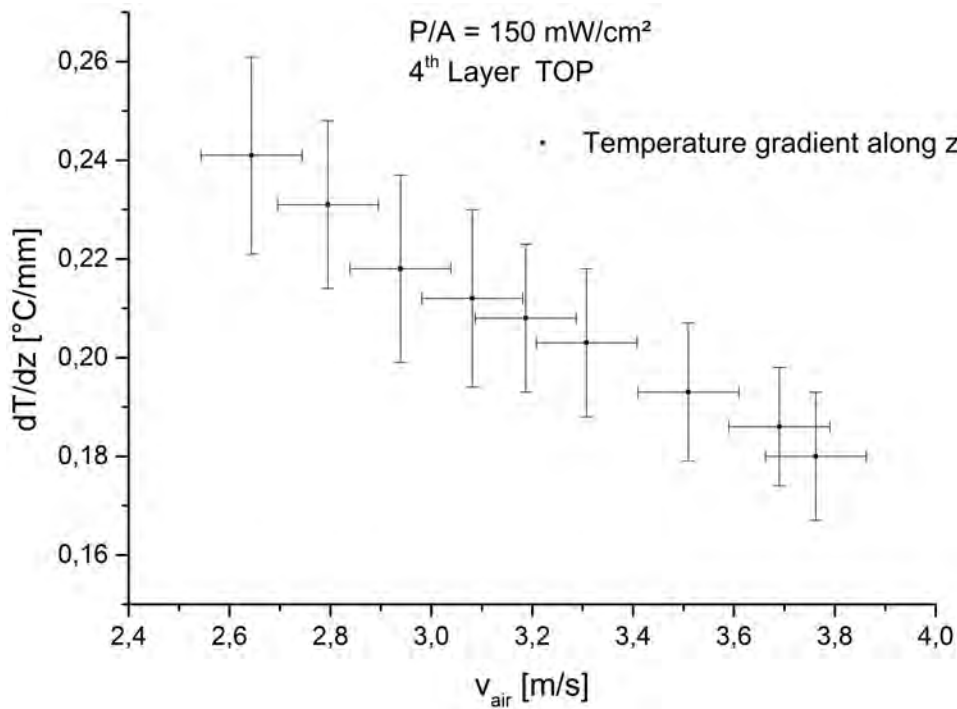


Figure 4.14: The temperature gradient on the top 4th layer dependent to the air speed.

5 Simulations

To make a theoretical prediction about cooling with a gaseous flow, fluid and thermodynamics are needed. In particular the velocity field $\vec{v}(\vec{x})$, the vectorial velocity in every point, has to be determined. This problem is described by the Navier-Stokes equation [10], which for incompressible fluids is given by:

$$\rho \frac{\partial}{\partial t} \vec{v} + \rho (\vec{v} \cdot \vec{\nabla}) \vec{v} = \rho \vec{\nabla} \Phi - \vec{\nabla} p + \eta \vec{\nabla}^2 \vec{v} \quad (5.1)$$

where ρ is the density of the fluid, Φ is the gravitational field, p is the pressure and η is the viscosity of the fluid¹. The assumption of a incompressible fluid simplifies the Navier-Stokes equation. Comparative simulations showed, that the effect of this assumption is small but saves a lot of computing time ($\Delta T_{comp} \approx \Delta T_{incomp} + 1^\circ\text{C}$ for the simulation with 2 m/s but more than double computing time). Incompressible fluids have the distinction of having a constant density ($\frac{\partial}{\partial t} \rho = 0$), so that with the continuity equation of fluid dynamics:

$$\frac{\partial \rho}{\partial t} + \vec{\nabla} (\rho \cdot \vec{v}) = 0 \quad (5.2)$$

the divergence of the velocity field vanishes: $\vec{\nabla} \cdot \vec{v} = 0$.

As the Navier-Stokes equation is non-linear chaotic phenomena known as turbulences can occur.

If there are solid state objects, the fluid has to flow around, as in our setup e.g. the heating foils, boundary conditions have to be taken into account. Especially the no-slip condition, meaning that the velocity on the solid surface has to be zero, defines flow and thermal boundary layers. The flow boundary layer describes a layer near the surface in which the gas velocity goes from zero (on the surface) to 99% of the velocity of the surrounding gas flow, while the thermal boundary layer is the layer in which the temperature changes from the surface temperature to the temperature at which 99%

¹More terms, like the Coriolis force, can be added, if there are more phenomena effecting the system.

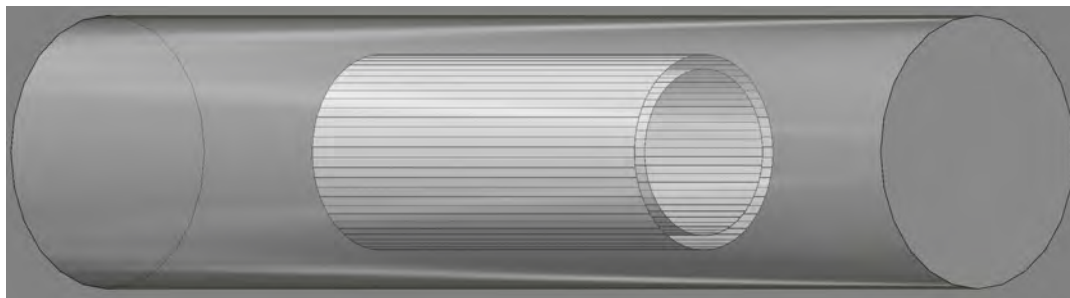


Figure 5.1: The CAD design for the CFD simulations.

of the temperature difference between the surface and the surrounding atmosphere is reached.

Since the geometry of the model is difficult to incorporate and the Navier-Stokes equation has to be solved numerically, it is reasonable to simulate the gas flow and heat exchange with a software which is specialized for it. The basic concept of this kind of simulation software, called CFD for Computational Fluid Dynamics, is to divide the solving for the full domain into a finite number of subdomains. This approach is called FEM for finite element method. The simulations I will describe and discuss in the following were performed with Autodesk[®] Simulation CFD 2014, which is available for free for students and faculty members. The CFD program has to be fed with a CAD model, which was created with Autodesk[®] AutoCAD 2014 and modified with Autodesk[®] Inventor Fusion 2013.

The goal of the simulations is to have a comparison between the measurement and simulation results for an air flow and then to estimate the advantages of helium with regards to air. The first design consisted of two (concentric) cylindrical Kapton[®]-aluminium layers which had the big disadvantage that a round shape is hard to mesh, so that the software created so many mesh-points, that the simulation needed almost all available memory of the PC and created huge files. Obviously also the time needed to simulate a scenario was fairly long. In order to reduce the mesh-points, without differing to much from the experimental setup, a 60-gons design was constructed². The 60-gon shape was chosen (instead of a 24- or 28-gon shape) in order to reconstruct the measurement model which has a round shape (see section 3.1). The CAD model is shown in Fig. 5.1. Both 60-gon consists of 25 μm Kapton[®] and 25 μm aluminium. They are 400 mm long and have approximately the same radii as the physical model and are surrounded by air or helium, which are enclosed by an acrylic cylinder. The thermal properties of aluminium,

²The computing time was reduced from about half a day per scenario to about an hour.

acrylic glass, air³ and helium³ were already contained in the CFD software, while the properties of Kapton[®] (looked up in [11]) were fed in manually. The layers are heating with 264 W resp. 321 W (see: Tab. 4.3). The inflowing gas (either air or helium) has a temperature of 20 °C and velocities⁴ between 0.5 m/s and 4 m/s. The results can be qualitatively analysed with thermal images and quantitatively with measurement points, positioned on the model. In order to check if the temperature converged, every scenario was run with initial temperatures of 100 °C and 0 °C. The differences of both simulations were used as estimation for the errors.

5.1 Simulations With Air

In order to illustrate the temperature distribution on the simulated model, thermal images (see Fig. 5.2) are helpful, but to compare the results of the simulation to the measurements temperature profiles and gas flow projections were extracted from the data.

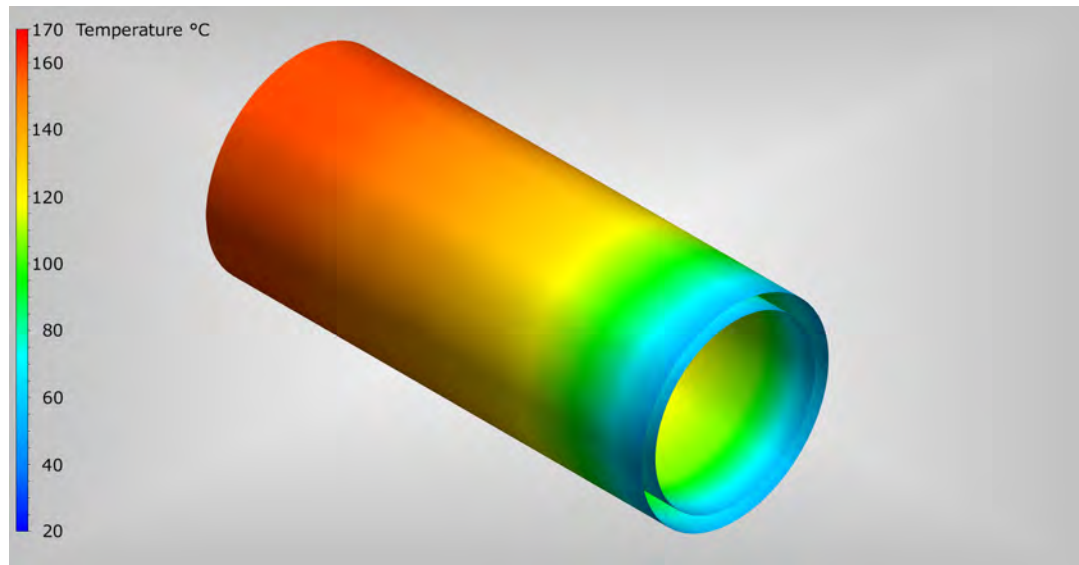
5.1.1 Temperature Profiles

The temperature profiles gained from the simulations with air flow are plotted in Fig. 5.3 and Fig. 5.4. One can immediately see that the profiles significantly differ from the measured ones. The temperature does not increase linearly as measured on the physical model. Instead the profile is similar to the predictions calculated for a flat single sensor, as it was done by Marco Zimmermann [3]. Diverse reasons may cause this discrepancy, the most obvious will lie in the difference between the flat CAD model and the physical model with all its extra edges and material for the frame.

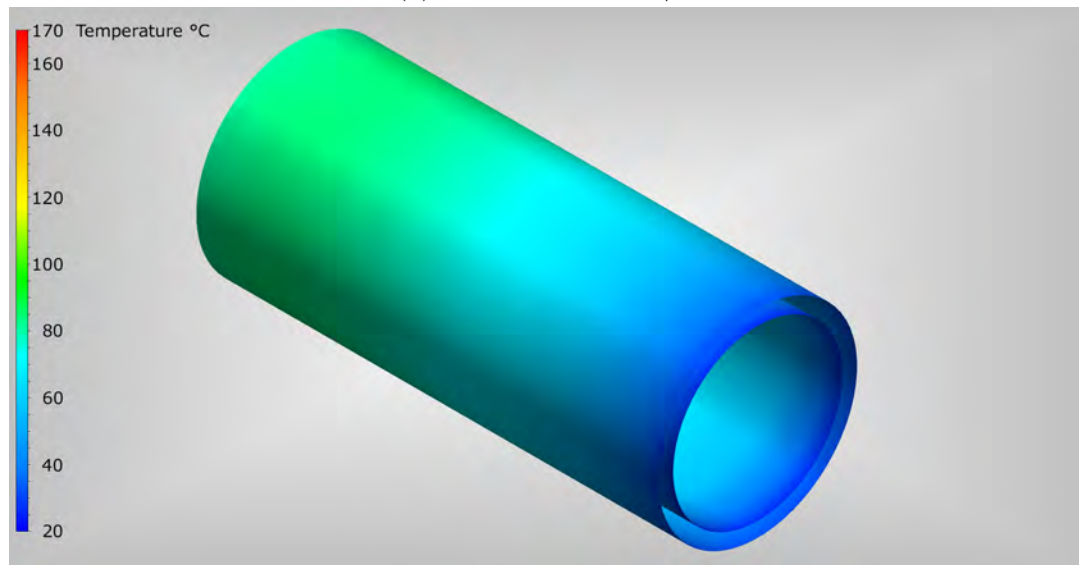
As it can already be seen in Fig. 5.2, the temperature seems to be roughly constant in φ direction this can be quantified by looking at the temperature profiles on top, side and bottom of the simulations for a single air speed (Fig. 5.5). This plot shows that the differences in φ are extreme small and also reveals that the 3rd layer is slightly hotter than the 4th at this particular airspeed.

³As well as the fluid properties.

⁴The mean velocity on the inlet cross-section.



(a) Air speed of 0.5 m/s.



(b) Air speed of 4.0 m/s.

Figure 5.2: Thermal images of the model cooled with air. For easy comparison the temperature range is the same in both images: from 20 °C to 170 °C.

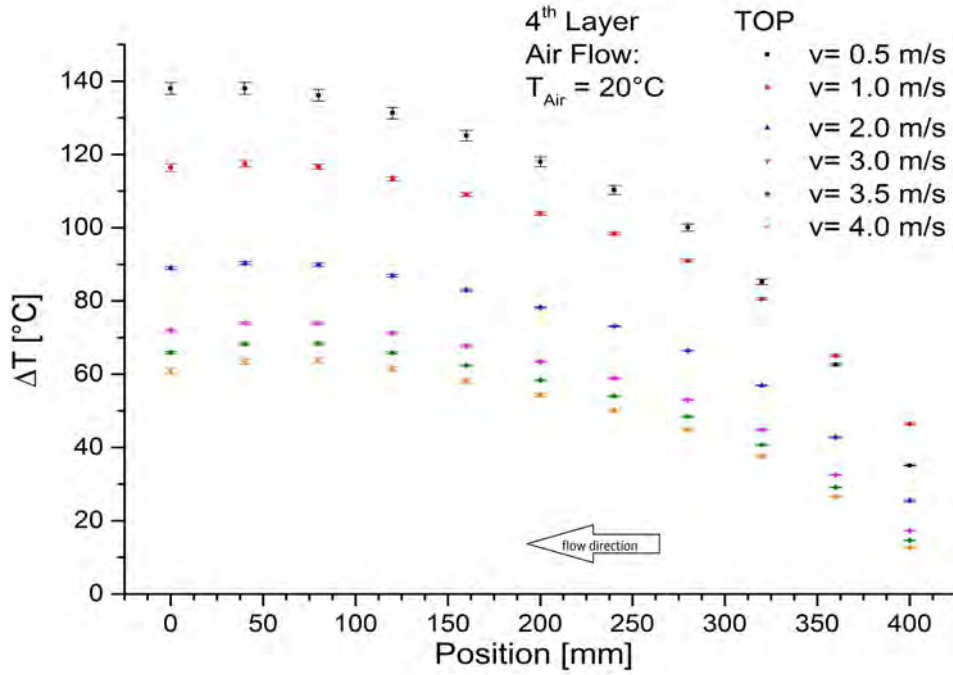


Figure 5.3: Temperature profiles on the 4th layer obtained from the simulations with air flow.

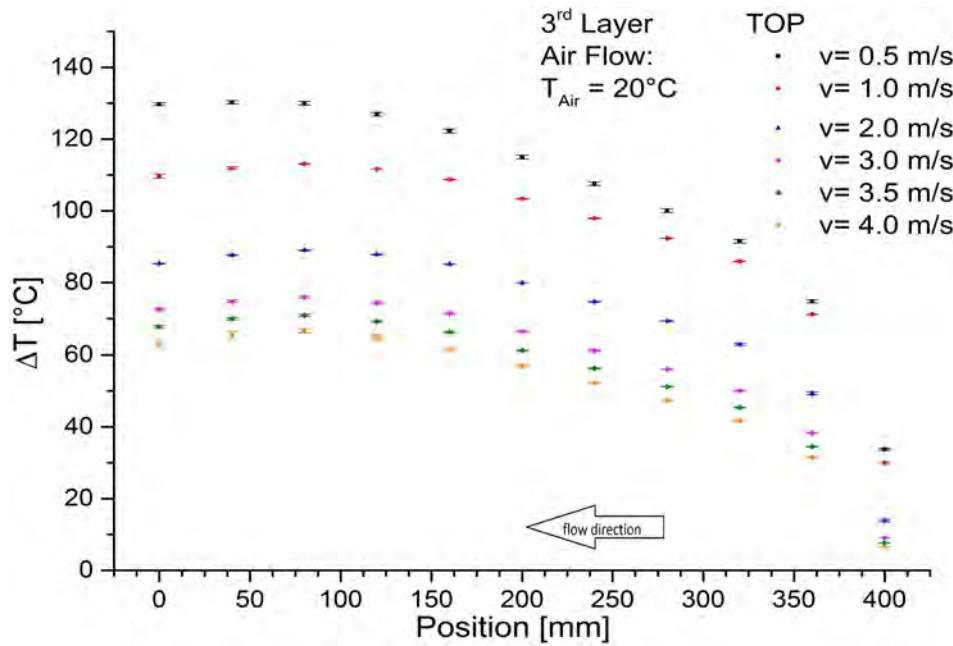


Figure 5.4: Temperature profiles on the 3rd layer obtained from the simulations with air flow.

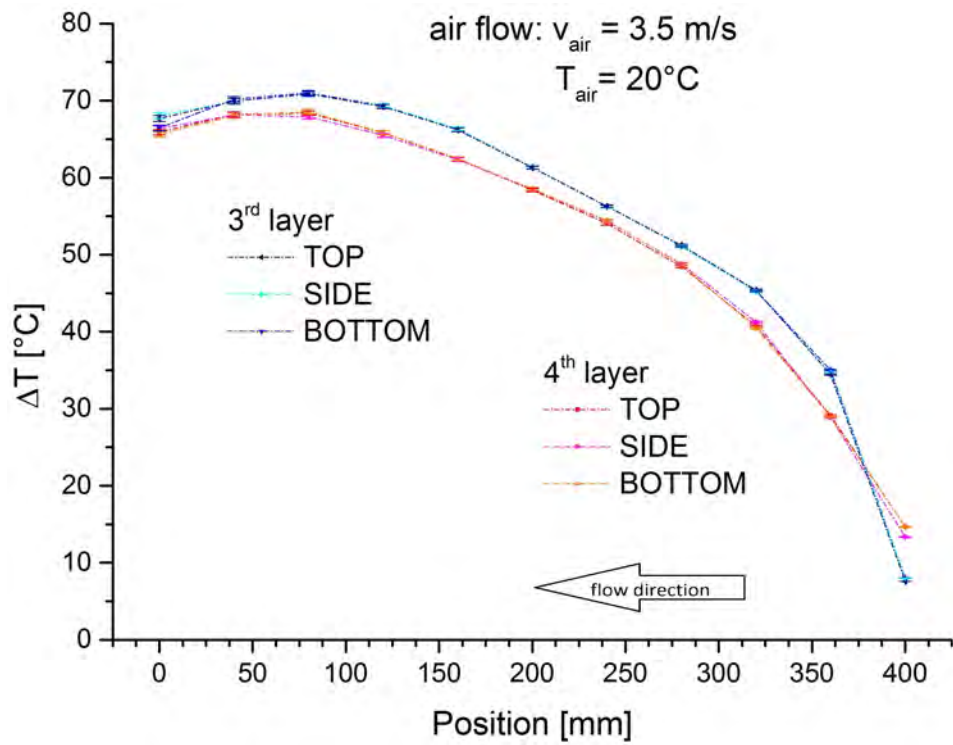


Figure 5.5: Temperature profiles on the 3rd and 4th layer on the top, side and bottom position at 3.5 m/s air speed.

5.1.2 Air Speed Projection

To again analyse the flow dependence of the temperature, projections on the air speed were made. Fig. 5.6 shows the air speed dependence of the maximum temperature on

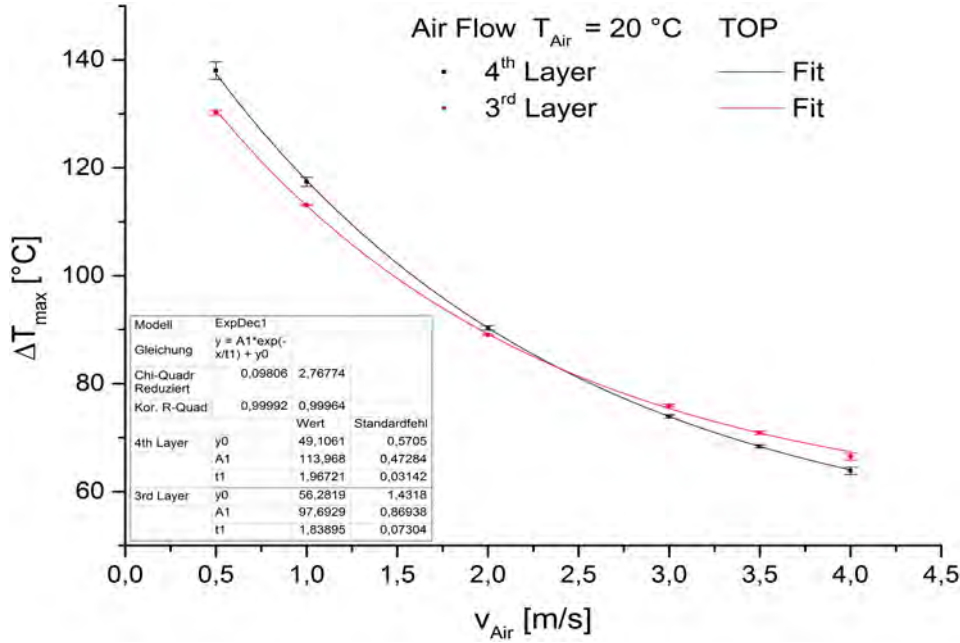


Figure 5.6: The maximum temperature on the top of the model in dependence of the air speed.

the top of both the 3rd and the 4th layer. Since for the simulations it was possible to go to lower air speeds and fixed speeds are defined, the behaviour can be analysed more clearly. An exponential decrease can be observed here, so that the data were fitted with a function of the form:

$$\Delta T_{max} = A \cdot e^{-\frac{v_{air}}{v}} + \Delta T_0 \tag{5.3}$$

where ΔT_{max} is the simulated maximum temperature on the model, A gives the extrapolated temperature (minus the offset) if no flow is applied, v_{air} is the air speed, v is the “decay constant” and ΔT_0 is the extrapolated temperature for extremely high air speeds. The validity of both extremal temperatures is fairly doubtful since other effects such as strong turbulences for higher velocities or more radiation cooling at higher temperatures will become dominant. Nevertheless, the “decay constant” v might be of interest for the comparison of helium and air cooling. For the 4th layer the fit gives $v = 1.97(4)\text{ m/s}$ and for the 3rd layer $v = 1.84(8)\text{ m/s}$ for air.

Furthermore, one can see that the temperature on the 3rd layer is lower than on the 4th layer for small air speeds, but higher for stronger air flows. This could not be observed in the measurements.

In order to compare the measurements to the simulations, the measured and simulated air speed dependence is illustrated in Fig. 5.7. It is to be taken into account that in

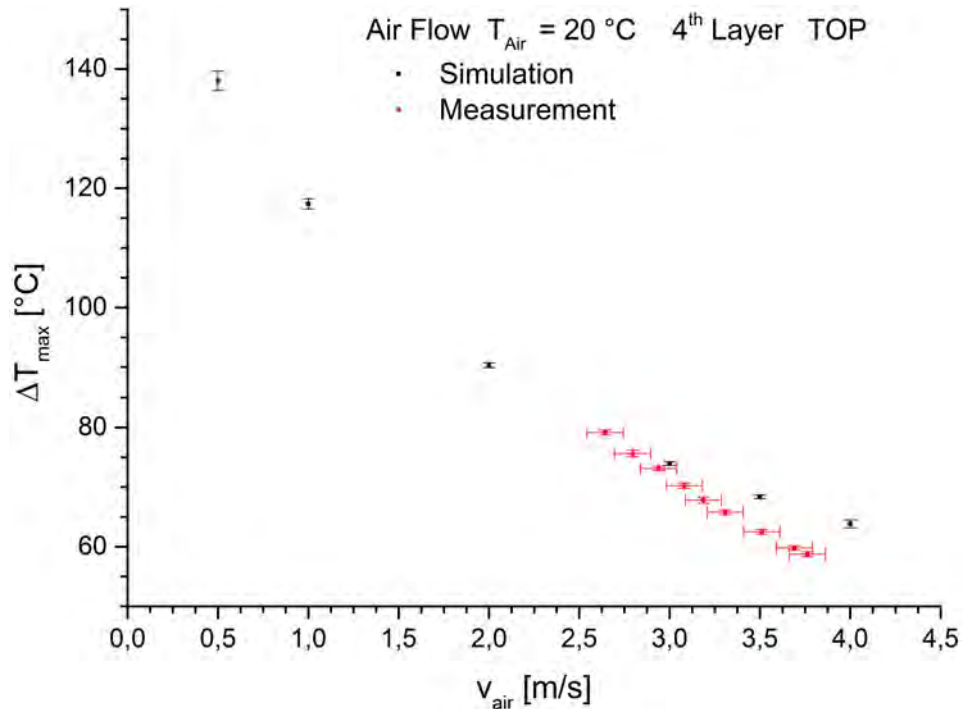


Figure 5.7: Comparison of maximum temperatures measured and simulated.

case of the simulation, the air speed v_{air} is the mean air velocity over inlet cross section, while in case of the measurements the maximum air speed was searched for. On the other hand the inlet cross section of the physical setup is smaller since the electric motor occupies space in the middle. Although the CAD model is quite coarse, the simulation results of the maximum temperatures match fairly well with the measurements. This is a nice finding, as it allows the use of the simulations to estimate the effects of helium cooling.

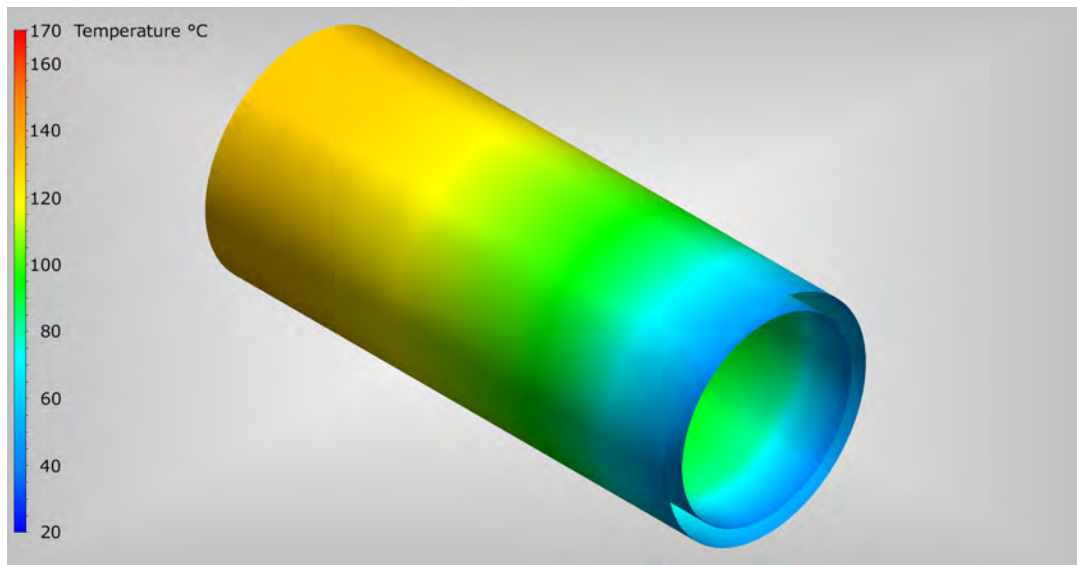
5.2 Simulations With Helium

As mentioned before, it is planned to operate the cooling of the detector with helium instead of air. This is on the one hand due to less coulomb scattering of particles in gases with low atomic number. On the other hand the low atomic mass number and

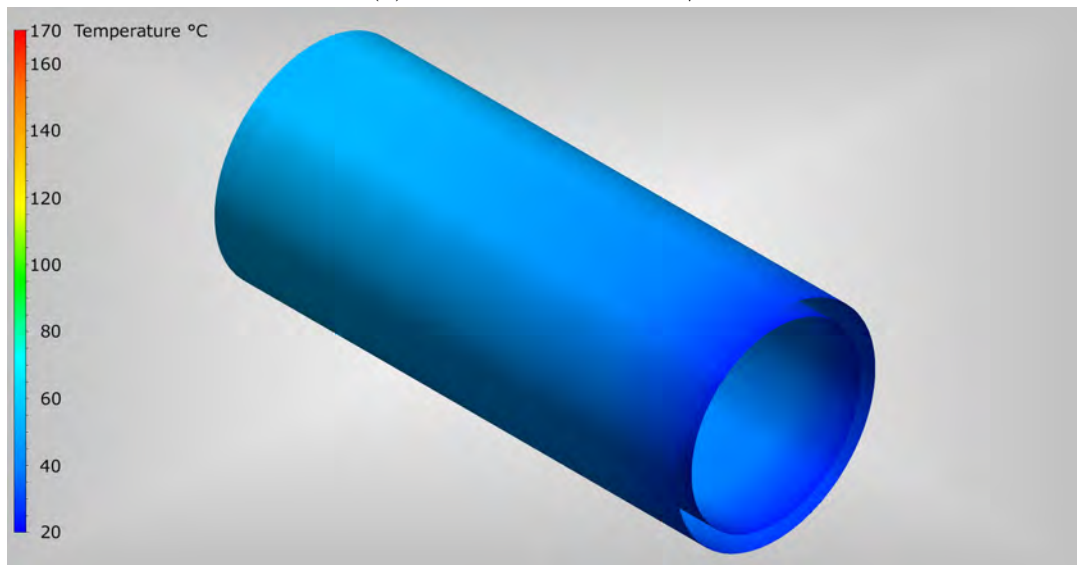
the fact that helium is a noble gas gives it thermal properties which are convenient for cooling by forced convection. Indeed, the heat capacity of helium is lower than of e.g. air (for equal volumes) but the heat conductivity is much better due to the lightness of the helium atoms. To estimate the advantages of helium compared with air, the simulations were also performed with helium. Fig. 5.8 shows the thermal images for two simulations with helium. The comparison with the simulations with air (Fig. 5.2) reveal at once that the cooling with helium is more effective. Again temperature profiles and velocity projections are shown for illustration.

5.2.1 Temperature Profiles

The temperature profiles obtained from the simulations with helium flow are plotted in Fig. 5.9 and Fig. 5.10. As one can see, the profiles look even flatter than the profiles from the air simulations. Additionally, the profiles on the 3rd and 4th layer again look fairly similar. To verify this and to analyse the behaviour in φ direction Fig. 5.11 is shown. Again the temperature variation in φ direction is very small. In contrast to the air simulation here, the 3rd layer is slightly hotter. The velocity projection illustrates this more precisely.



(a) Helium speed of 0.5 m/s.



(b) Helium speed of 4.0 m/s.

Figure 5.8: Thermal images of the model cooled with helium. For easy comparison the temperature range is the same as for the air cooling before: from 20 °C to 170 °C.

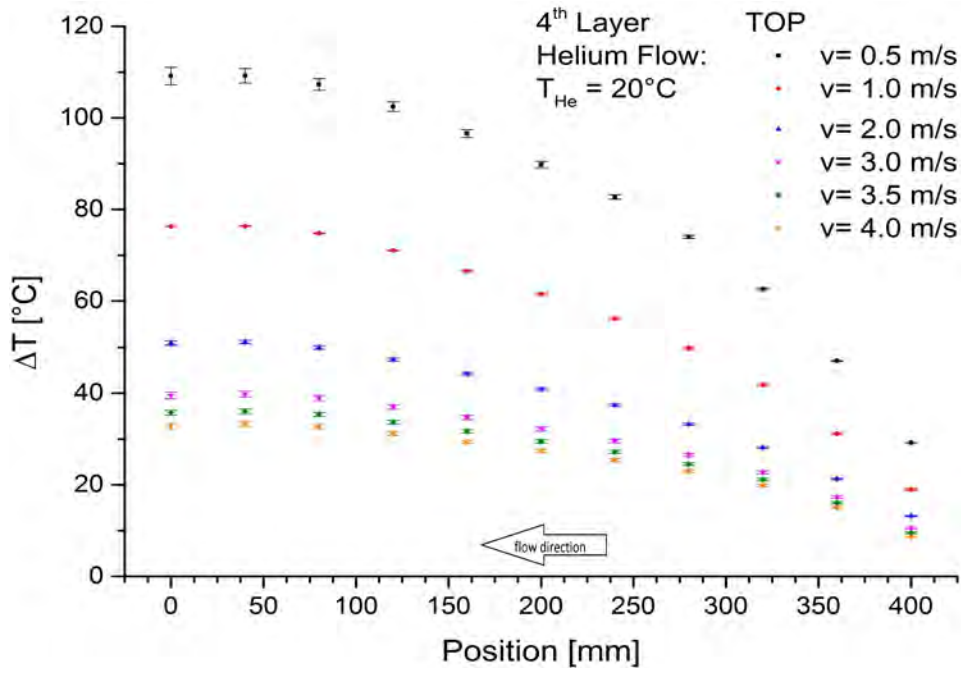


Figure 5.9: Temperature profiles on the 4th layer obtained from the simulations with helium flow.

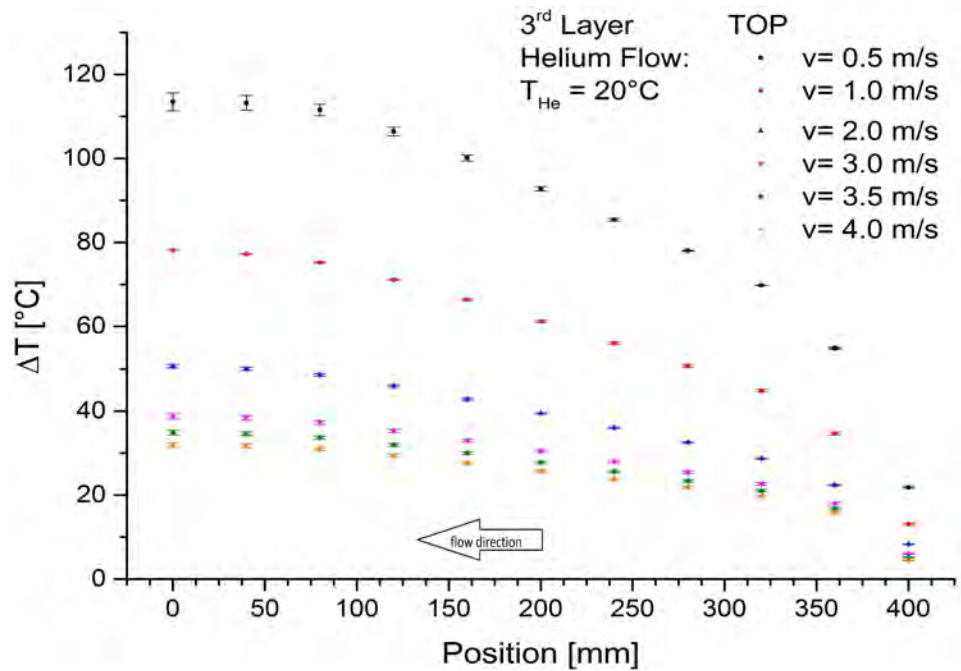


Figure 5.10: Temperature profiles on the 3rd layer obtained from the simulations with helium flow.

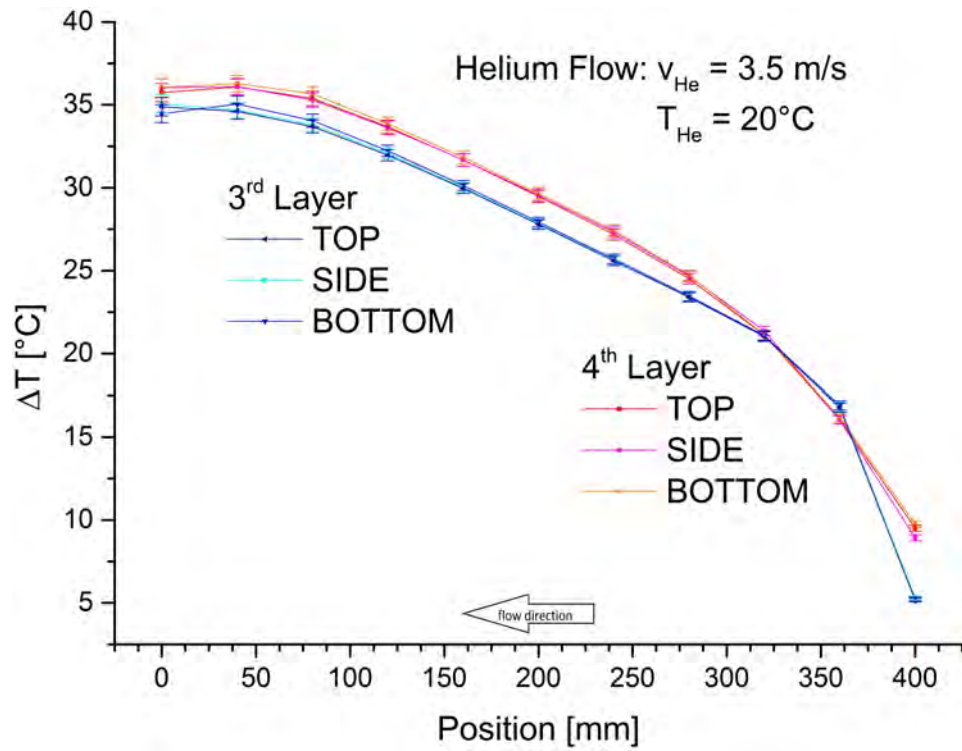


Figure 5.11: Temperature profiles on the 3rd and 4th layer on the top, side and bottom position at 3.5 m/s helium speed.

5.2.2 Helium Speed Projection

Fig. 5.12 shows the flow dependence of the maximum temperature of the model while cooled with helium. The decrease of the temperature with helium cooling differs signifi-

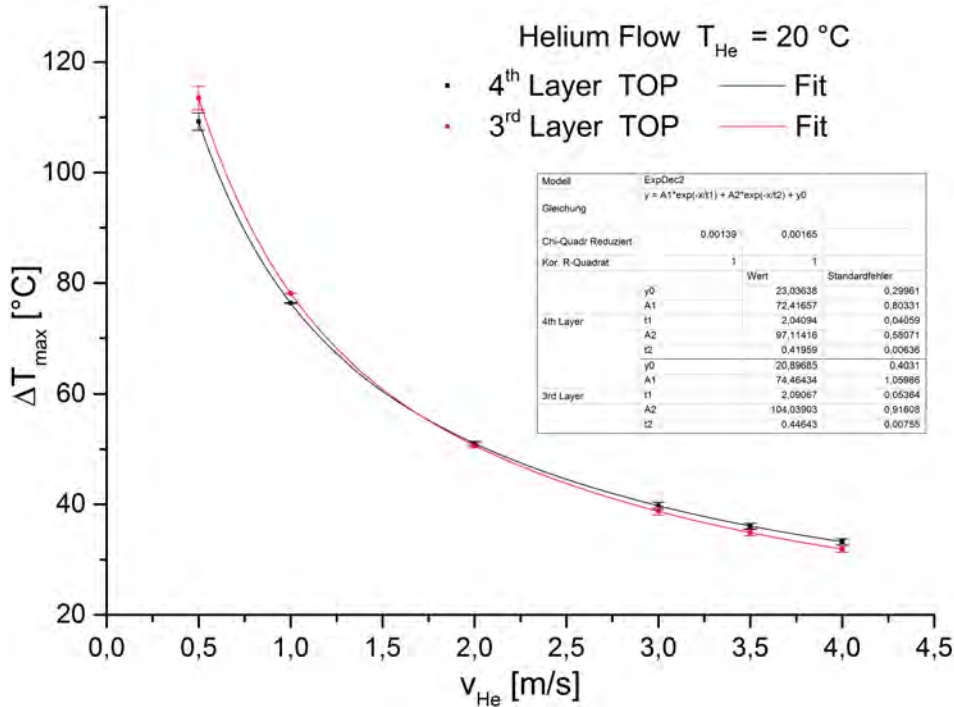


Figure 5.12: The maximum temperature on the top of the model in dependence of the helium speed.

cantly from the air cooling. For the air cooling the decrease could be well described with a single exponential function, while for the helium cooling this is not sufficient. Instead, two exponential functions are needed, so that the fit function looks like:

$$\Delta T_{max} = A_1 \cdot e^{-\frac{v_{He}}{v_1}} + A_2 \cdot e^{-\frac{v_{He}}{v_2}} + \Delta T_0 \tag{5.4}$$

The parameters are listed in Tab. 5.1. Compared with the air simulation, the temperature drops faster with increasing helium speed at low velocities but then decreases similarly for higher speeds. Furthermore, the temperature is systematically lower while cooling with helium instead of air.

	4 th layer		3 rd layer	
	Value	Error	Value	Error
A_1 [°C]	72.42	0.81	74.46	1.06
A_2 [°C]	97.11	0.59	104.04	0.92
ΔT_0 [°C]	23.04	0.30	20.90	0.41
v_1 [m/s]	2.041	0.041	2.091	0.054
v_2 [m/s]	0.4196	0.0064	0.4464	0.0076

Table 5.1: Fit parameters.

5.3 Comparison

In section 5.1 it was found that the measurements and simulations with air match fairly well taking into account simplifications applied to the CAD model. This gives the opportunity to also compare the simulations with helium to both other results. Fig. 5.13 shows the comparison of measurement and simulation results. As one can see, the simulations with helium give much lower temperatures than reached with air cooling. According to these results, one can either reach lower temperatures while cooling with helium at similar flow speeds or can reduce the velocities if it is required to prevent vibrations of the Kapton[®]-frame or a combination of both.

Fig. 5.14 shows temperature profiles obtained from simulations with air and with helium at an exemplary flow speed of 3.0 m/s. As mentioned before the profile of the helium cooling is flatter than the air cooling profile which derive from the lower maximum temperature.

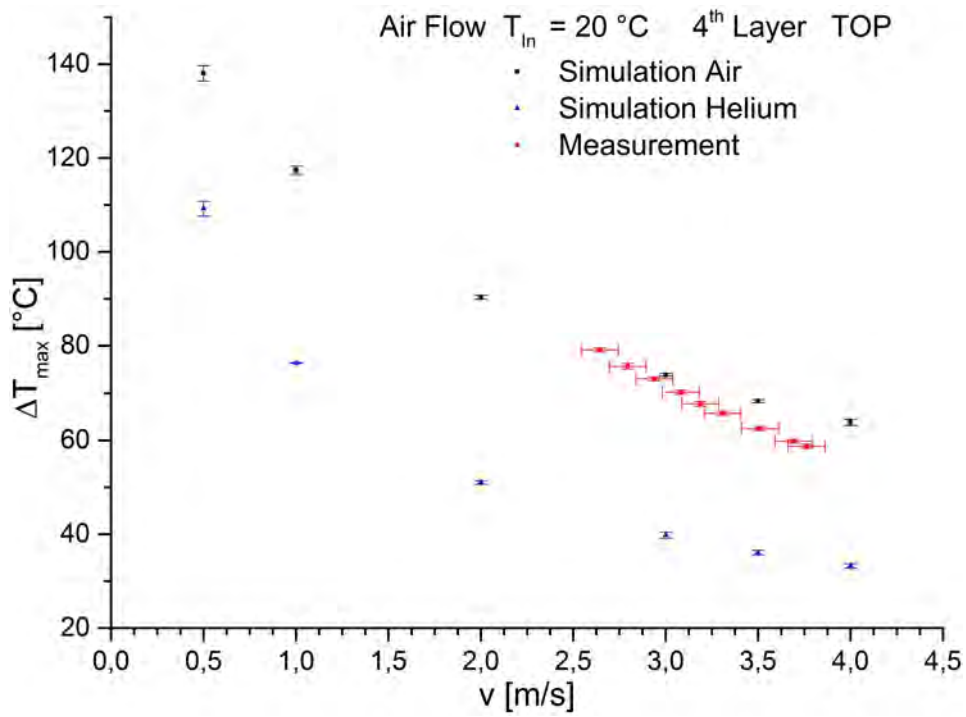


Figure 5.13: Comparison of the flow speed and medium dependence of the maximum temperature.

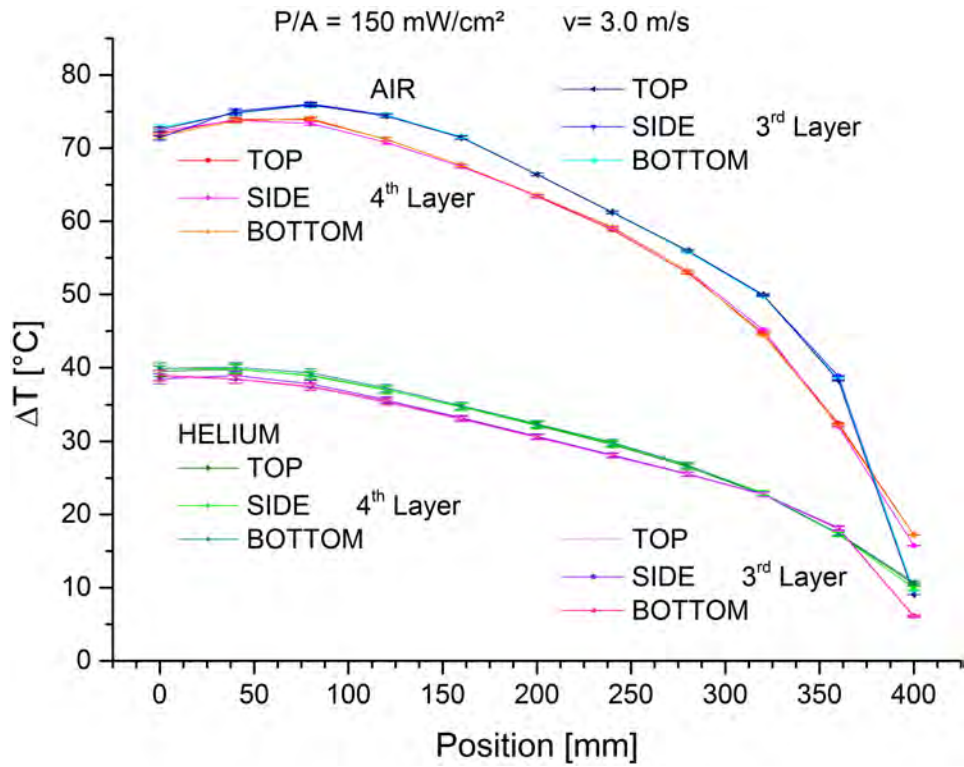
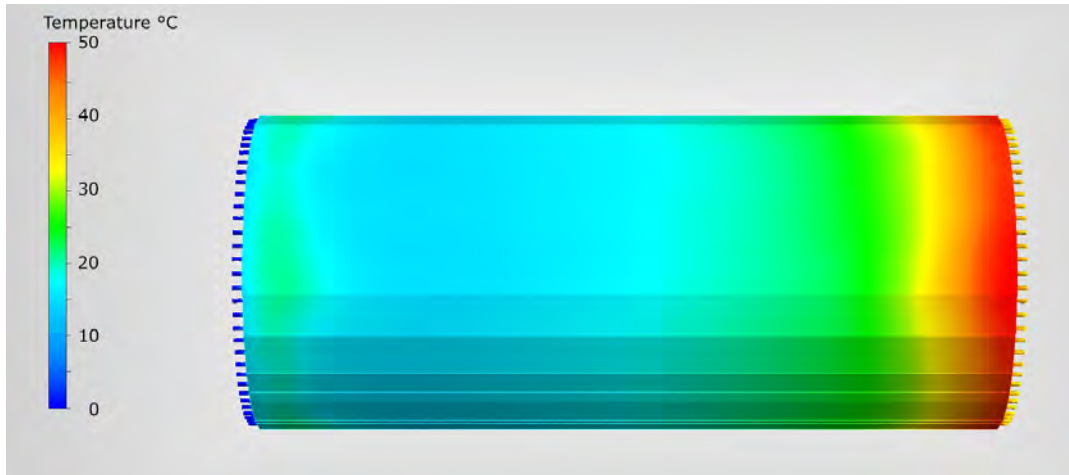
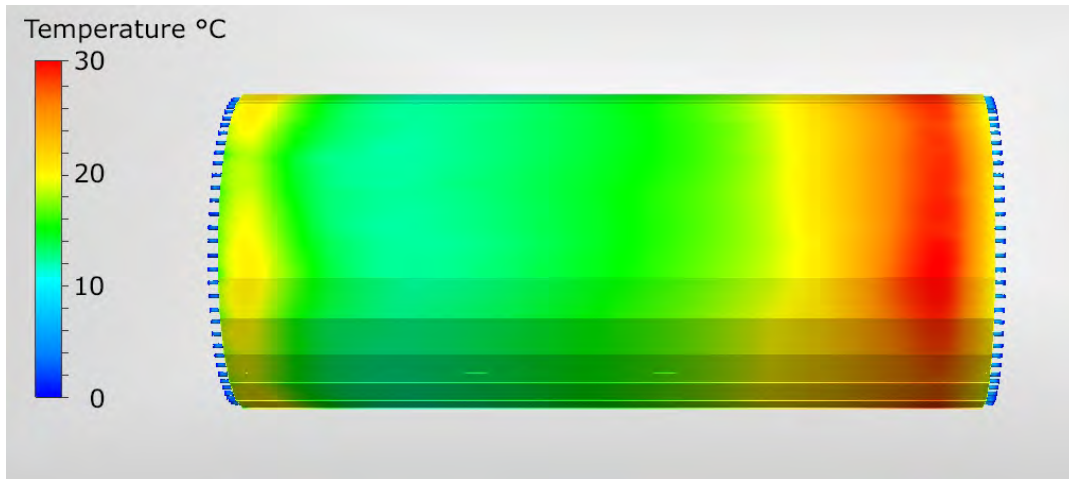


Figure 5.14: Comparison of temperature profiles obtained from simulations with air and with helium.

5.4 Further Simulations



(a) In ducts: 1 m/s in the opposite direction as the main flow. Beside ducts: 1 m/s in the same direction as the main flow.



(b) In ducts: 5 m/s in the opposite direction as the main flow. Beside ducts: 5 m/s in the opposite direction as the main flow.

Figure 5.15: Thermal images of the more detailed 3^{rd} layer model, heating with 150 mW/cm^2 and cooled with a main helium flow of 0.5 m/s and additional flows in and beside the ducts.

Fig. 5.15 gives a little outlook how the temperature distribution may look like when the Kapton[®]-ducts are used for additional cooling flows. These thermal images show the 3^{rd} layer heating with 150 mW/cm^2 and cooled with 0°C helium flows. The main flow outside the ducts runs from the left to the right here with only 0.5 m/s . Fig. 5.15a results from additional flows in the ducts directed against the main flow with inlet helium speed of 1 m/s and additional flows beside the ducts in the same direction as the main flow

with also 1 m/s inlet speed. Fig. 5.15b results from additional flows in the ducts directed against the main flow with inlet helium speed of 5 m/s and additional flows beside the ducts also directed against the main flow with also 5 m/s inlet speed. The 4th layer is missing in both scenarios. More simulations on the more detailed model including the 4th layer are required.

6 Conclusion and Outlook

The Mu3e experiments intends to search for the charged lepton flavour violating decay $\mu \rightarrow eee$ which is forbidden in the original formulation of the Standard Model of particle physics and suppressed to unobservable levels in its extended formulations. According to some theories beyond the SM the $\mu \rightarrow eee$ decay is allowed with branching ratios greater than $BR(\mu \rightarrow eee) > 10^{-16}$. Since the Mu3e experiment aims to reach a sensitivity of $< 10^{-16}$ at 90 % confidence level the decay could be found which then would be a great indication of physics beyond the SM.

In order to reach this huge sensitivity a detector is designed based on HV-MAPS. These pixel sensors have many advantages, especially they can be thinned down to 50 μm reducing multiple scattering and have integrated readout electronics making additional readout chips in the active detector volume unnecessary. This integrated electronics brings along the disadvantage that they will consume about 150 mW/cm^2 . Since the power consumption sums up to about 3 kW for the complete detector, it is obvious that this released heat has to be carried away actively. This has to be done with a gaseous flow since fluids would nullify the big advantage of the low scattering of the HV-MAPS.

For estimating the possibilities of cooling with gaseous helium so far two studies have been carried out. First the cooling was studied on a setup simulating a single sensor. The next step was to investigate the cooling on a bigger structure of the detector. This is documented in this thesis.

In order to investigate the cooling of the detector substructure, a heatable model was created. The constructed model is able to endure more than 500 W heating power (while a cooling flow is applied), sufficient to simulate the heat generation of the HV-MAPS on the 3rd and 4th layer of the Mu3e pixel detector. It is assembled from heatable foils consisting of Kapton[®] and aluminium patterns which form heating wires, a frame and a flow reactor. For now, the cooling was performed with an air flow. Additionally, computer simulations were performed.

The cooling tests with air were very successful. At full heating power and applied air flow of 20 °C and e.g. 3.5 m/s absolute temperatures of 85 °C were measured.

The successful comparison of measurements and simulations with air and the simulations with helium give the base for the assumption that the helium cooling of the detector should be sufficient. According to the measurements, temperatures lower than 70 °C can already be reached with air of 0 °C and speeds of slightly more than 3 m/s. With helium cooling this should be possible at even lower flow speed, as the simulations showed. Besides no mechanical vibrations were visible on the heating foils, even at air speeds of almost 4 m/s.

The actual model works fine, as a first approach to investigate the gaseous cooling of the Mu3e detector though it is necessary to do further investigations. First of all, measurements in a helium atmosphere should give more indications of how much better the helium cooling is compared with the air cooling. Furthermore the used model does not include the Kapton[®]-ducts on the inside of the layers which should bring along the opportunity of reducing the temperature gradients by applying helium flows in the ducts in opposite direction to the helium flow around the whole detector. Mechanically, the model differs significantly from the proposed detector design, making it difficult to predict the mechanical stability of a Kapton[®]-frame in a gas flow. Therefore also tests with mechanical prototypes are required.

In conclusion, this thesis justifies the assumption, that the Mu3e detector can be cooled down to reasonable operating temperatures with a gaseous helium flow.

Bibliography

- [1] A. Blondel et al., “*Research Proposal for an Experiment to Search for the Decay $\mu \rightarrow eee$* ”, ArXiv e-prints, January 2013, (arXiv:1301.6113 [physics.ins-det]).
- [2] U. Bellgardt et al., [SINDRUM Collaboration], “*Search for the Decay $\mu^+ \rightarrow e^+e^+e^-$* ”, Nucl.Phys., **B299** 1, 1988.
- [3] M. Zimmermann, *Cooling with Gaseous Helium for the Mu3e Experiment*, Bachelor thesis, Heidelberg University, 2012.
- [4] J. Beringer et al., [Particle Data Group], “*Review of Particle Physics (RPP)*”, Phys.Rev., **D86** 010001, 2012.
- [5] M. Kiehn, *Track Fitting with Broken Lines for the MU3E Experiment*, Diploma thesis, Heidelberg University, 2012.
- [6] aluMATTER, Laser absorption coefficients.
- [7] JUMO GmbH & Co. KG, *Aufbau und Anwendung von Platin-Temperatursensoren*.
- [8] Labfacility, *Pt1000 Elements, Thin Film (1000 Ohm)*.
- [9] P. v. Walter, *LogicBox V4.1*, 2013.
- [10] D. Meschede, *Gerthsen Physik*, Springer-Lehrbuch ; SpringerLink : Bücher. Springer Berlin Heidelberg, Berlin, Heidelberg, 24., revised edition, 2010.
- [11] DuPontTM High Performance Films, *Kapton[®] Polyimide Film*, 2012.

7 Acknowledgements

An dieser Stelle möchte ich meine Dank an alle die los werden, die mich während des Studiums, aber auch insbesondere während dieser Bachelorarbeit unterstützt haben. Besonders möchte ich mich bei Dr. Niklaus Berger bedanken, der mich während meiner Arbeit und vor allem während der Schreibphase sehr unterstützt hat und diese Arbeit auch beurteilt. Ebenso möchte ich mich bei Prof. Uwer bedanken, der sich bereiterklärt hat diese Arbeit als Zweitkorrektor zu bewerten. Auch stand mir Dr. Dirk Wiedner immer mit einem guten Rat zur Seite, weshalb auch ihm mein besondere Dank gilt. Bei Prof. Schöning sowie allen Mitgliedern der Mu3e Arbeitsgruppe möchte ich mich für die wirklich sehr angenehme Arbeitsatmosphäre und Hilfsbereitschaft bedanken.

Ganz besonders möchte ich mich auch bei meiner ganzen Familie und meiner Freundin bedanken, die mich immer und in jeglicher Hinsicht unterstützen.

Erklärung

Ich versichere, dass ich diese Arbeit selbstständig verfasst und keine anderen als die angegebenen Quellen und Hilfsmittel benutzt habe.

Heidelberg, den 14.02.2014, Lukas Heinz Georg Huxold